

7N-02
198969
P-51

TECHNICAL NOTE

D-373

AN INVESTIGATION OF INDUCED-PRESSURE PHENOMENA ON AXIALLY
SYMMETRIC, FLOW-ALINED, CYLINDRICAL MODELS EQUIPPED
WITH DIFFERENT NOSE SHAPES AT FREE-STREAM MACH
NUMBERS FROM 15.6 TO 21 IN HELIUM

By James N. Mueller, William H. Close,
and Arthur Henderson, Jr.

Langley Research Center
Langley Field, Va.

(NASA-TN-D-373) AN INVESTIGATION OF
INDUCED-PRESSURE PHENOMENA ON AXIALLY
SYMMETRIC, FLOW-ALINED, CYLINDRICAL MODELS
EQUIPPED WITH DIFFERENT NOSE SHAPES AT
FREE-STREAM MACH NUMBERS FROM 15.6 TO 21 IN

N89-71138

Unclass

00/02 0198969

NATIONAL AERONAUTICS AND SPACE ADMINISTRATION
WASHINGTON

May 1960

NATIONAL AERONAUTICS AND SPACE ADMINISTRATION

TECHNICAL NOTE D-373

AN INVESTIGATION OF INDUCED-PRESSURE PHENOMENA ON AXIALLY
SYMMETRIC, FLOW-ALINED, CYLINDRICAL MODELS EQUIPPED
WITH DIFFERENT NOSE SHAPES AT FREE-STREAM MACH
NUMBERS FROM 15.6 TO 21 IN HELIUM

By James N. Mueller, William H. Close,
and Arthur Henderson, Jr.

SUMMARY

Induced-pressure-distribution studies were made and schlieren photographs were taken at free-stream Mach numbers from 15.6 to 21 in helium flow of axially symmetric, flow-alined, cylindrical models equipped with different nose shapes. The nose shapes were a hemisphere, a 45° included-angle cone, a 90° included-angle cone, a hemispherically blunted 45° included-angle cone, a hemisphere modified by a 90° included-angle conical tip, and a flat configuration. Static-pressure orifices were located along the cylindrical surface of the models from zero body diameters to 50 body diameters downstream of the nose-cylinder juncture.

An analysis of the data showed that the highest induced pressures were measured on the bluntest (flat nose) configuration; as the nose shapes decreased in bluntness, the induced pressures also decreased. Beyond 20 model diameters from the nose-cylinder juncture the induced pressures became essentially independent of the degree of nose bluntness. The induced pressures correlate on the basis of blast-wave-theory parameters; thus, the induced pressures are a function of nose drag but are essentially independent of nose shape beyond 1 model diameter downstream of the models' shoulders.

Unmodified blast-wave theory is inadequate for predicting induced pressures except in very limited regions. A modified form of blast-wave theory was shown to give good agreement with experimental results when experimentally determined viscous effects were incorporated. Comparison of experimental induced pressures and shock shapes obtained on 90° conical-tip configurations with characteristics-theory calculations for similar configurations shows good agreement. A significant result which indicates the usefulness of attached shock calculative methods was that the experimental induced pressures on the pointed hemisphere and hemisphere configurations were essentially equal when the nose drag coefficients of the models were essentially equal.

Tests of Reynolds number effects (0.0625 to 0.32×10^6 in a 2-inch helium tunnel at the Langley Research Center and 0.062 to 0.75×10^6 in the Langley 11-inch hypersonic tunnel) showed that the magnitudes of the induced pressures at a short distance downstream of the shoulder exhibited a strong dependence on Reynolds number. Beyond 5 model diameters the induced pressures showed negligible change for a 12-fold increase in Reynolds number.

Data obtained in a conical-flow (Mach number gradient) nozzle and reduced by a buoyancy-method technique (NACA Research Memorandum L52H21) are shown to agree with data obtained in a uniform-flow (zero Mach number gradient) nozzle.

INTRODUCTION

The fluid-dynamics phenomena associated with flight at hypersonic speeds have been the subject of intensive research in recent years. In this research domain one problem that has received considerable attention has been the cause and effects of induced pressures. Although induced-pressure effects exist at all speeds, not until hypersonic speeds are reached (Mach number $\gg 1$) do these effects become of primary importance. It is well known that at hypersonic speeds large pressure gradients can be induced on plates and body surfaces without the plates or bodies themselves having any inclination with the undisturbed free-stream direction. These induced-pressure gradients behind blunt-nose bodies are largely the result of the disturbances created by bodies in inviscid flow which are reflected from the shock back onto the afterbody, coupled with the large entropy and vorticity gradients which occur in the shock layer. Much effective work has been done and is being done in the analysis and solution of this problem. Reference 1 traces the history of the induced-pressure problem, and some representative papers relating to this problem are also included herein (refs. 2 to 11).

Inasmuch as the whole development of the boundary layer and the induced-pressure field may depend to some extent upon the conditions around the nose or the leading-edge region of a hypervelocity vehicle, the present investigation was initiated to study the effects of nose shape on induced pressures over three-dimensional, flow-aligned, cylindrical bodies at free-stream Mach numbers from 15.6 to 21 in helium flow. The nose shapes used in this investigation included a hemisphere, a 45° included-angle cone, a 90° included-angle cone, a hemispherically blunted 45° included-angle cone, a hemisphere modified by a 90° included-angle conical tip, and a flat configuration.

The primary objective of this investigation was to determine the effect of nose shape on induced pressures; tests for this phase were made

at a free-stream Mach number of 21. A secondary objective, though of no less importance, was to assess the Reynolds number effect on induced pressures on blunt bodies. These tests were made with hemisphere-cylinder models in both a 2-inch helium tunnel and the Langley 11-inch hypersonic tunnel over a Mach number range from 15.6 to 21 and a Reynolds number range from 0.062 to 0.75×10^6 .

The present paper presents the results of this investigation. A comparison of the present data with data obtained on similar configurations in different helium facilities is also included.

SYMBOLS

$C_{D,n}$	nose drag coefficient
d	model diameter
G	Mach number variation with x_n/t
M	Mach number
p	static pressure
p'	corrected static pressure, $p + (p_{\infty,n} - p_{\infty,l})$
R_d	Reynolds number based on free-stream conditions and diameter of test models
s	model surface distance downstream from stagnation point
T	temperature
t	thickness
x	model axial distance downstream
y	vertical distance from model axis
γ	ratio of specific heats
θ	wedge angle

Subscripts:

l	local conditions
max	maximum
n	nose of model
s	shoulder of model
t	stagnation conditions
∞	free-stream conditions

1
8
4
8

APPARATUS AND TESTS

2-Inch Helium Tunnel

Most of the tests were performed in a 2-inch-diameter helium tunnel at the Langley Research Center. A schematic diagram of the tunnel and its operating components is shown in figure 1. Helium was supplied from a 67-cubic-foot reservoir to the tunnel stagnation chamber at pressures up to 3,000 lb/sq in. gage. The tunnel could be operated continuously for periods in excess of 10 minutes at a stagnation pressure of 2,000 lb/sq in. gage. The calibration of the axisymmetric tunnel (no windows) is shown in figure 2. A more detailed description of this facility is included in reference 1.

Visual observations (schlieren photographs) of all the basic test models were made in a modified version of the 2-inch helium tunnel which was the same as the original tunnel except that the test section was equipped with schlieren windows. This modification consisted of slicing the tunnel walls to accommodate the flat, plate-glass windows. The disturbances from the windows do not affect the test-section flow in the region of interest, as determined from flow calibrations.

Models and model support.- Six basic test models were used in this investigation. The models were 0.090-inch-diameter cylinders 5 inches long equipped with various nose shapes, as shown in figure 3. Pressures were measured at each of 12 longitudinal orifice locations given in table I. A photograph of the basic test models is shown as figure 4.

The test models were supported by means of a long sting whose longitudinal position was controlled by a motorized gear and screw system (fig. 1). The model-sting arrangement is shown in figure 3.

Instrumentation and accuracy.- Supply pressures were measured on a Bourdon gage with an accuracy of ± 5 lb/sq in. Static pressures were read on a U-tube butyl phthalate manometer. The reference pressure on the U-tube manometer was maintained at less than 20 microns of mercury (approximately 0.01 inch of butyl phthalate). This reference pressure was considered to be within the reading accuracy of the U-tube. The estimated accuracy of the measured static pressures was ± 0.0007 lb/sq in. The estimated accuracy of the tunnel calibrated Mach number, in the region in which the test models were positioned, was about 0.8 to 1.0 percent.

Tests.- All tests in the 2-inch helium tunnel were made at a tunnel reservoir pressure of 2,000 lb/sq in. gage. This pressure is equivalent to a Reynolds number of 0.694×10^6 per inch, or 0.0625×10^6 if the model diameter is used as the characteristic flow length.

For all tests, the models were alined along the tunnel center line at zero angle of attack and zero angle of yaw. Since a longitudinal Mach number gradient of about 0.7 per inch existed in the 2-inch helium tunnel, the models were positioned longitudinally in the tunnel so that the shoulders of the models were alined with the nozzle station where $M_\infty = 21$. This value was considered the reference Mach number for the tests. Since the orifices on the models were located with reference to the shoulder, corresponding orifices on different models were located at the same longitudinal test-section stations. An analysis of the longitudinal Mach number gradient effect upon the measured pressures is presented in the section entitled "Reduction of Data."

The small size of the models required a test procedure which permitted pressure measurements at only one orifice station per test. The test sequence was to measure the pressure at the rearmost orifice ($x_s/d = 50$), close this orifice with solder, and drill a new one slightly upstream on the model surface. This process was repeated with a separate test for each orifice location until data for the most forward orifice station were obtained. All orifices were 0.030 inch in diameter.

The surface static pressures were recorded manually at the steady-state condition, which was usually obtained about 90 to 120 seconds after the test was started.

Langley 11-Inch Hypersonic Tunnel

Some of the data included in this report were obtained from tests in the Langley 11-inch hypersonic tunnel by using an axisymmetric contoured Mach number 18 helium nozzle. Helium was supplied to the tunnel stagnation chamber at pressures from 200 to 1,600 lb/sq in. absolute.

The test Mach number varied from 15.6 at a stagnation pressure of 200 lb/sq in. absolute to 18.1 at a stagnation pressure of 1,600 lb/sq in. absolute. The Mach number gradient along the longitudinal axis of the test section was less than 0.05 per inch at all stagnation pressures. A partial calibration of this nozzle may be found in reference 12. The average operating time for these tests was approximately 15 seconds.

Models and model support.- The details of the two hemisphere-cylinder models which were tested in this facility are given in table II. Both models were approximately 19 inches long and were mounted on a streamlined, gear-driven strut protruding from the floor of the tunnel several inches behind the test section. The models were tested at zero angle of attack and zero angle of yaw with the nose located 4 inches ahead of the center line of the test section.

Instrumentation.- Pressures were recorded on mechanical, optical pressure recorders. Because of the short duration of a test the recorded pressures did not always reach steady-state conditions and these data have been omitted from this presentation.

Test procedures.- Three separate test procedures were utilized during the tests in this facility to determine the effects of outgassing (i.e., increased recorded pressure due to vapor and/or air molecules being slowly released from the pores of the inner tubing wall) and the effects of using long lengths of plastic tubing in the orifice-to-instrument system (such as increased outgassing and possible minute leakage due to porosity).

In method 1, no attempt was made to outgas the system. Approximately 3-foot lengths of plastic tubing were used to connect the stainless-steel tubing (silver soldered flush to the model surface to form the orifices) and the recording instruments.

In method 2, pretest outgassing was employed and the long lengths of plastic tubing were replaced with steel tubing. Only short lengths of this plastic tubing were used to facilitate flexible joining of metal tubes in the system. Electrical tape was used to seal the orifices and the entire orifice-to-instrument system was evacuated to approximately 50 microns of mercury and held at this pressure overnight. Shortly before the test the vacuum pumps were stopped and the tape over the orifices was removed. The system was thus exposed to atmospheric pressure for a period of not more than 3 minutes.

In method 3, in-test outgassing was employed. In order to determine whether pretest outgassing was sufficient, a more elaborate method was used so that the orifice-to-instrument system was not at any time

subjected to a pressure higher than anticipated steady-state flow pressure. This technique was achieved by evacuating the orifice-to-instrument system (as was done for pretest outgassing) to a pressure of approximately 15 microns of mercury. Shortly before each test the valves to the vacuum pumps were closed, but the tape over the orifices remained in place, sealing the orifice-to-instrument system at this low pressure. The tape was then removed from the orifices only after flow was fully established. This eliminated any possibility of outgassing during the recording phase of the test.

A comparison of data obtained by these three methods is shown in figure 5. The data obtained with long plastic tubing in the system and with no precautions taken to eliminate errors due to outgassing (method 1) show large deviations from the data obtained by using either of the two methods intended to eliminate outgassing errors. It is, therefore, concluded that long lengths of plastic tubing should not be used when attempts are made to measure very low pressures and that precautions must be taken to insure the absence of any outgassing error.

As the data obtained by using methods 2 and 3 are essentially the same, all data presented herein from the Langley 11-inch hypersonic tunnel and the 2-inch helium tunnel were obtained by using the more practical test technique of method 2 (pretest outgassing) unless otherwise noted.

REDUCTION OF DATA

The conical nozzle of the 2-inch helium tunnel produces flow with both a longitudinal Mach number gradient and a conical flow angularity which is zero on the center line and increases to a maximum at the edge of the test region. In order to obtain a first-order indication of the most desirable method of presenting the data, a theoretical analysis was performed on a sharp-nose and a blunt-nose two-dimensional model in a flow field with a linearly varying Mach number by means of the method of characteristics for $\gamma = 5/3$. This analysis did not include the variation of flow angularity which occurs in a real conical flow.

The free-stream Mach number distribution was represented by

$$M_{\infty} = M_{\infty,n} + G \frac{x_n}{t} \quad (1)$$

where x_n/t is measured from the nose of the model, and G is the variation of Mach number with x_n/t . Surface pressures were calculated on both shapes for $M_{\infty,n} = 11.5$ and 25 and $G = 0, 0.02$, and 0.04 for each value of $M_{\infty,n}$. The configurations used in the study are shown in figure 6. The initial wedge angle of the sharp shape was 14° for all values of $M_{\infty,n}$. For the blunt shape the wedge angle was varied with $M_{\infty,n}$ so that M was 1 on the surface.

Figure 6 shows the shock shape and some representative characteristic lines for both configurations at $M_{\infty,n} = 25$. The characteristic lines have been drawn straight for simplicity, although in general they are curved. Shock-shape results are presented for the $G = 0$ case only, since the variation of shock shape with Mach number gradient was insignificant for the scope of this investigation. It can be seen that the region of the shock through which the effect of any external disturbance (such as free-stream Mach number gradient) can be felt on the body is well forward of the maximum downstream extent of the affected portion of the body. This, of course, results because of the low Mach angle. Note the downstream extent to which disturbances and reflections originating in the high vorticity region (region of high shock curvature) of the shock from the blunt-nose shape are felt.

The pressure distributions on the models in the flow with a Mach number gradient have been reduced by three methods and are compared with the pressure distribution in terms of p/p_{∞} for the constant Mach number case in figure 7. The constant Mach number curve was used as the criterion by which the adequacy of the proposed data-reduction methods for $G > 0$ was judged. The data-reduction methods used were as follows:

Method 1 - This method is based on the simple pressure ratio

$$p/p_{\infty,n}$$

where p is the calculated body surface pressure and $p_{\infty,n}$ is the free-stream pressure at the nose. Method 1 is conventionally used in zero Mach number gradient flow. (This method was used in ref. 1.)

Method 2 - This method is also based on a simple pressure ratio

$$p/p_{\infty,l}$$

where $p_{\infty,l}$ is the local free-stream static pressure that would exist at the point in the flow where p is calculated if the body were not present. Method 2 has been suggested as a means of accounting for the effects of Mach number gradient on surface pressures.

Method 3 - This method based on a buoyancy-correction technique is represented by the following pressure-ratio expression:

$$p'/p_{\infty,n} = \frac{p + (p_{\infty,n} - p_{\infty,l})}{p_{\infty,n}}$$

Method 3 has been used successfully at supersonic speeds to correct the pressure drag of bodies which were tested in flow with a slight longitudinal pressure gradient. (See ref. 13.)

Figure 7 illustrates the effect of Mach number, Mach number gradient, and model configuration on surface pressures and shows that in all cases methods 1 and 3 are superior to method 2, within the scope of this investigation. Note also that the accuracy of all corrections is better on the blunt model than on the sharp one.

Since method 3 is consistently the best method at both Mach numbers for the sharp shape and as good as or better than method 1 for the blunt shape at the Mach numbers of this investigation, method 3 was used to reduce the data obtained in this investigation, unless otherwise noted.

As mentioned previously, the results of the analysis are exact only for zero flow angle. Recent unpublished calculations in the Langley 11-inch hypersonic tunnel, which include flow angularity, indicate that the level of the curves shown in figure 7 may be considerably lowered; the amount of shift increases with increasing angularity and increasing x_n/t . However, the buoyancy correction method (method 3) is even better than shown and is superior to the other two methods in all cases considered herein. For larger values of G however, this correction is inadequate.

RESULTS AND DISCUSSION

Pressure Distributions

Basic data.- The basic pressure data obtained on the six primary test models of this investigation are shown in figure 8. The data are presented in the form of the corrected measured static pressure p' on the model, nondimensionalized by the free-stream static pressure at the nose of the model $p_{\infty,n}$. This pressure parameter is plotted as a function of the orifice location downstream of the model shoulder referenced to the model diameter. Several observations can be made from these data. The highest induced pressure measured at the station nearest the shoulders of the models occurred on the hemispherical-nose model. The flat-nose model and the 90° cone model had higher induced pressures than the hemisphere farther downstream and would be considered more blunt than the hemisphere; however, at the most forward orifice location their induced pressures were lower than for the hemisphere. The reason that the pressures near the shoulder are lower for the flat face and the 90° cone than for the hemisphere is due to the fact that a corner expansion takes place at the shoulder on the two models with a sharp-edge shoulder and this has the effect of lowering the pressure in the region near the shoulder. An analysis was made in which the simple Prandtl-Meyer expansion technique was used and the pressures were calculated by expanding the flow on a hemisphere from the sonic point to the shoulder and by using a corner expansion for the 90° cone. This analysis indicated that the pressures were less on a 90° cone.

The pressure distribution for the flat-nose configuration shown in figure 8 illustrates the type of pressure distribution that occurs for a model with a sharp-edge shoulder. This distribution of pressure just downstream of the model shoulder is characteristic of flat-nose configurations. As pointed out in reference 2, the expansion followed by compression waves returning from the sonic line and expansion waves returning from the shock wave cause, respectively, a low pressure immediately after the corner, an increase in pressure, and then the final pressure decay. It is noted in figure 8 that the pressures on the various models far downstream of the models' shoulders are at a value which is about two times ambient pressure. Another point of interest noted in figure 8 is that the pressure gradients on the various models become nearly constant beyond 20 model diameters downstream of the shoulder.

Effect of Reynolds number.- The primary tests of this investigation were made in a 2-inch helium tunnel at $R_d = 0.0625 \times 10^6$. In order to investigate the effects of Reynolds number, a short program of

measuring induced pressures on the hemisphere-cylinder models of various diameters was undertaken and the results are shown in figure 9(a). The greatest variation of measured induced pressures with Reynolds number occurred in the region nearest the shoulder. Figure 9(a) shows that the induced pressures increase with decreasing Reynolds number; this might be expected because of the increased viscous effects at the lower Reynolds numbers. At a short distance downstream of the shoulder, $x_s/d = 0.5$, and with further increase in x_s/d all except the lowest Reynolds number data indicate only small differences in p'/p_{max} with variation in Reynolds number. The lowest Reynolds number data, on the other hand, display a significant difference from the higher Reynolds number data; however, the tendency of the lowest Reynolds number data to coalesce with the higher Reynolds number data as x_s/d is increased results in small to negligible difference in induced pressures at $x_s/d \approx 5.5$ for the Reynolds number range shown.

An additional program was undertaken in the Langley 11-inch hypersonic tunnel in which the Reynolds number was varied over a wide range by changing both the geometric scale of the model and the stagnation pressure. The models were $3/8$ and 1 inch in diameter and were tested at $0.062 \times 10^6 < R_d < 0.75 \times 10^6$ at $M_\infty = 15.6$ to $M = 18.1$. Some basic results from this program are shown in figure 9(b). These results essentially confirm the results obtained in the 2-inch helium tunnel. The results obtained from both facilities are summarized in figure 10. At $x_s/d = 5.56$ the measured induced pressures show little change for a 12-fold increase in Reynolds number. It should be noted (fig. 10), however, that even at the highest Reynolds number of this investigation Reynolds number effects are still very much in evidence at body stations x_s/d up to and including 1.39.

Effect of nose shape.— The induced pressures measured on the basic test models of this investigation are shown in figure 11. The level of induced pressures varies from a minimum to a maximum as the nose shapes are, respectively, changed from an essentially sharp nose shape (45° cone) to one which is blunt (flat). Also, the induced pressures become essentially independent of the degree of nose bluntness beyond about 20 model diameters downstream of the models' shoulders ($x_s/d = 20$).

All the nose shapes tested in this investigation were aerodynamically blunt except the 45° cone. According to blast-wave theory (ref. 6) the induced pressures on blunt-nose bodies should correlate when plotted against the parameter $\frac{x_s/d}{M_\infty^2 C_D^{1/2}}$. Figure 12 shows the

amenability of the present test results to correlation by this blast-wave-theory parameter. From figure 12 it may be seen that the induced pressures for all the configurations, in general, correlate very well. This result is particularly significant in view of the large range of nose-drag-coefficient values ($C_{D,n} = 0.316$ to 1.76) among the various test configurations and indicates a wide applicability of the correlative parameters. The correlation also indicates that the induced pressures are dependent on nose drag but are essentially independent of nose shape beyond $x_s/d \approx 1$ (i.e., $\frac{x_s/d}{M_\infty^2 C_D^{1/2}} = 0.002$).

Nose drag coefficients $C_{D,n}$ were based on pressures obtained from (1) exact-cone-theory computations for the 45° and 90° cones, (2) modified Newtonian theory for the hemisphere and flat-nose configurations, and (3) the generalized Newtonian theory of reference 14 for the modified hemisphere and the 45° blunt cone.

Comparison of experiment with theoretical predictions.- In figure 13 the experimental data obtained on the hemisphere-nose models are compared with results obtained by the blast-wave theory (developed in refs. 6, 15, 16, 17, 18, and 19) and also with those obtained by a modified blast-wave theory presented in reference 20. It appears that the unmodified-blast-wave-theory prediction of the induced pressures is good in the region (x_s/d location) in which it would be expected to apply - that is, not too close to the nose of the body (or origin of the blast) yet not so far downstream that the shock strength has decayed to a level where strong shock approximations no longer apply. However, this good agreement must be regarded as being, in part, fortuitous since the unmodified-blast-wave-theory prediction is for inviscid flow and the data are known to contain significant viscous effects. These viscous effects would alter the location of the region of agreement. Subject to these limitations, the region of applicability in the present case appears to be roughly from $x_s/d \approx 4$ to $x_s/d \approx 12$. This narrow region of adequate prediction by unmodified blast-wave theory makes the usefulness of the theory extremely limited for quantitative prediction of induced pressures, although its correlating form has much broader application as shown in figure 12.

As pointed out in reference 20, the deficiencies of the blast-wave theory have led to attempts to improve its range of applicability with different modifications. One modification is to shift the point of origin of the blast in order to improve predictions near the leading edge or nose (refs. 6 and 21); another modification is used to improve the agreement far downstream by assuming that the predicted surface pressure p is the pressure increment $p - p_\infty$ (ref. 19).

Love's method (ref. 20), which can also be considered a modification of blast-wave theory, is expressed by the following equation:

$$\frac{p'}{p_{\max}} = \left(\frac{1}{1 + x_s/d} \right) \frac{p_s}{p_{\max}} + \left(\frac{1}{1 + \frac{1}{x_s/d}} \right)^{p_s/p_{\infty}} \frac{p_{\infty}}{p_{\max}} \quad (2)$$

This equation is plotted in figure 13 for $M_{\infty} = 21$ and includes p_s/p_{\max} as predicted by Wagner (ref. 22). In contrast to the agreement between the predictions by equation (2) and experimental results for Mach numbers near 10 and less shown in reference 20, there is considerable disagreement between present experimental results near Mach 20 and the predicted values. However, there is excellent prediction of the trend of the experimental pressure decay. The large disparity between the magnitudes of the experimental and predicted pressures is attributed, for the most part, to the fact that the prediction is for inviscid flow. With increasing Mach number, viscous effects would become more important. These effects would distort the effective body shape in the vicinity of the nose and effectively enlarge the body. This distortion would shift the apparent shoulder of the body farther downstream. It has previously been shown (fig. 10) that the surface pressures are significantly affected by viscous effects up to $x_s/d \approx 1\frac{1}{2}$ and through the R_d range of these tests. At large downstream distances the experimental pressures do not reach ambient pressure as predicted for inviscid flow but reach a pressure which is about twice the ambient pressure. (See fig. 8.) Since a cone semiapex angle of only about $1\frac{30}{4}$ produces a pressure ratio of 2 on the cone surface at the Mach number of these tests, it appears reasonable that the experimental pressures at large downstream distances which are twice the ambient pressure are caused by this boundary-layer growth effect.

In an effort to examine the adequacy of equation (2) when viscous effects are included, the results of the present study have been used to obtain the experimental value of p_s/p_{\max} (fig. 10, at $x_s/d = 0$), and the experimental value of p_{∞}/p_{\max} far downstream (taken as twice the ambient pressure). The case examined is $M_{\infty} = 21$ and $R_d = 0.0625 \times 10^6$. When these values of p_s/p_{\max} and p_{∞}/p_{\max} , and the resulting value of p_s/p_{∞} , are incorporated in equation (2), the resulting prediction which includes viscous effects is in excellent agreement with the experimental results, as shown in figure 13. Thus,

if the values of these pressure ratios in viscous flow can be accurately obtained or predicted, equation (2) appears adequate for predicting induced pressures.

Figure 14 shows further comparisons of the experimental induced pressures with predictions calculated by the method of characteristics. Included for comparison are a 90° cone model, a hemisphere model, and a modified hemisphere model. The modified hemisphere model has a 90° conical tip added to its nose. The calculated induced pressures and the experimental induced pressures for the 90° cone model are in good agreement. Likewise, good agreement is shown between calculated and experimental pressures for the modified hemisphere.

The fact that hemisphere and modified hemisphere experimental data are essentially equal emphasizes the usefulness of attached shock calculative methods, such as the characteristics theory, for induced-pressure predictions.

Shock Shapes

Schlieren flow photographs were taken of the models, and the shock shapes were measured with an optical comparator. In figures 15 to 20 the shock shapes for the six basic test models ($d = 0.090$ inch) of this investigation are shown. In each figure a schlieren photograph of the model is shown in part (a), the coordinates of the shock wave are shown in part (b), and the shock coordinates nondimensionalized by the model diameter and plotted on a logarithmic scale are shown in part (c). The empirical equation describing the shock is shown in each figure. Comparison of the empirical shock equations obtained for the hemisphere and flat-nose configurations of this investigation with those obtained for the same type of bodies in reference 2 shows favorable agreement. Figure 21 shows the results obtained on two flat-nose configurations of two different diameters.

The shock-wave shapes of the hemisphere and modified hemisphere are compared with the calculated (method of characteristics) shock-wave shape of the modified hemisphere in figure 22. The agreement is considered good.

Comparison With Other Experimental Data

In figure 23 some induced-pressure data obtained on hemisphere-cylinder configurations in the present investigation are compared with published data obtained on similar configurations in the Princeton

University helium hypersonic tunnel (ref. 2)¹. The data are uncorrected for Mach number gradient because of the large differences in the values of G that existed for the different facilities and of the uncertainty as to how to correct data when G is large (0.26 for the Princeton facility).

The differences that exist between the 2-inch helium-tunnel data and the 11-inch hypersonic-tunnel data have been previously discussed and appear to be primarily a result of Reynolds number effect in the range $\frac{x_s}{d} = 0$ to $\frac{x_s}{d} \approx 5\frac{1}{2}$. The Princeton data for $M_\infty = 16.9$ show excellent agreement with the Langley 11-inch hypersonic-tunnel data, with the exception of the last data point shown plotted at 8 diameters downstream of the model shoulder. The Princeton data for $M_\infty = 18.8$, however, exhibit considerable disagreement with the data of this investigation beyond about 3 model diameters downstream of the model shoulder. Some of the possible reasons for the disagreement are as follows: (a) the value of G was several times larger in the Princeton tests than in the present tests, (b) the quality of the flow in the test region for $M_\infty = 18.8$ may have affected the results, and (c) the pressure level is lower at $M_\infty = 18.8$ than at $M_\infty = 16.9$, and the results are thus more susceptible to any outgassing or plastic-tubing-porosity effects that may have existed.

CONCLUSIONS

An investigation of induced-pressure phenomena has been made at free-stream Mach numbers M_∞ from 15.6 to 21 in helium flow on axially symmetric, flow-aligned, cylindrical models which differed in nose shape. Nose shapes tested were a hemisphere, a 45° included-angle cone, a 90° included-angle cone, a hemispherically blunted 45° included-angle cone, a hemisphere modified by a 90° included-angle conical tip, and a flat configuration. An analysis of the data indicated the following conclusions:

1. The effects of outgassing and the use of plastic tubing on the measured pressures can be of quite large magnitudes, but with precautions these effects can be eliminated.

¹The Princeton tunnel data published in reference 2 in the form of $C_p/C_{p_{\max}}$ have been converted to the uncorrected form p/p_{\max} (for comparative purposes) by use of a tunnel Mach number calibration curve furnished the Langley Research Center through the courtesy of Dr. S. M. Bogdonoff of the Princeton University staff.

2. A theoretical analysis by means of the method of characteristics has shown that data obtained on both sharp- and blunt-nose two-dimensional configurations in flow with a free-stream Mach number gradient can be satisfactorily reduced to represent data on the same model in flow with zero Mach number gradient provided the product of free-stream Mach number gradient and model thickness is small. Comparison of experimental results on hemisphere-cylinder models in the 2-inch helium tunnel, with a Mach number of 21 at the nose and a Mach number gradient of about 0.7 per inch, and in the 11-inch hypersonic constant Mach number tunnel ($15.6 \leq M_\infty \leq 18.1$) verifies this conclusion.

3. Tests of Reynolds number effects (0.0625 to 0.32×10^6 in a 2-inch helium tunnel and 0.062 to 0.75×10^6 in the Langley 11-inch hypersonic tunnel) showed that the induced pressures at a short distance downstream of the shoulder exhibited a strong dependence on Reynolds number. Beyond 5 model diameters, however, the induced pressures showed negligible change for a 12-fold increase in Reynolds number.

4. The highest induced pressures were measured on the bluntest (flat-nose) configurations; as the nose shapes decreased in bluntness, the induced pressures also decreased. Beyond 20 model diameters from the nose-cylinder juncture the induced pressures became essentially independent of the degree of nose bluntness.

5. The induced pressures correlate on the basis of blast-wave-theory parameters; thus, the induced pressures are a function of nose drag but are essentially independent of nose shape beyond 1 model diameter downstream of the shoulder.

6. Unmodified blast-wave theory is inadequate for predicting induced pressures except in very limited regions. A modified form of blast-wave theory was shown to give good agreement with experimental results when experimentally determined viscous effects were incorporated.

7. Comparison of experimental induced pressures and shock shapes obtained on 90° conical-tip configurations with characteristics-theory calculations for similar configurations shows good agreement.

8. The induced pressures on the hemisphere-cylinder model show a negligible change when the hemispherical nose is modified by the addition of a 90° conical tip and the nose drag coefficients of the models remain essentially equal. This result is particularly significant since it indicates the usefulness of attached shock calculative methods.

Langley Research Center,
National Aeronautics and Space Administration,
Langley Field, Va., January 29, 1960.

L
8
4
8

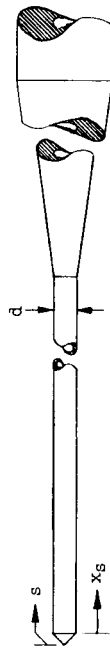
REFERENCES

1. Henderson, Arthur, Jr., and Johnston, Patrick J.: Fluid-Dynamic Properties of Some Simple Sharp- and Blunt-Nosed Shapes at Mach Numbers From 16 to 24 in Helium Flow. NASA MEMO 5-8-59L, 1959.
2. Vas, I. E., Bogdonoff, S. M., and Hammitt, A. G.: An Experimental Investigation of the Flow Over Simple Two-Dimensional and Axial Symmetric Bodies at Hypersonic Speeds. Rep. No. 382 (WADC TN 57-246), Dept. Aero. Eng., Princeton Univ., June 1957.
3. Bogdonoff, S. M., and Vas, I. E.: Preliminary Study of the Flow Over a Blunt Flat Plate at Various Angles of Attack at $M = 13.3$ - Part II: Study of an Elliptical Leading Edge. Rep. No. D143-978-005 (ARDC-TR-56-41, ASTIA AD-113 079), Bell Aircraft Corp., Oct. 1, 1956.
4. Oliver, Robert E.: An Experimental Investigation of Flow Over Simple Blunt Bodies at a Nominal Mach Number of 5.8. GALCIT Memo. No. 26 (Contract No. DA-04-495-Ord-19), June 1, 1955.
5. Lees, Lester: Inviscid Hypersonic Flow Over Blunt-Nosed Slender Bodies. GALCIT Hypersonic Res. Proj. Memo. No. 31 (Contract No. DA-04-495-Ord-19), Feb. 1, 1956.
6. Lees, Lester, and Kubota, Toshi: Inviscid Hypersonic Flow Over Blunt-Nosed Slender Bodies. Jour. Aero. Sci., vol. 24, no. 3, Mar. 1957, pp. 195-202.
7. Ferri, Antonio, and Pallone, Adrian: Note on the Flow Fields on the Rear Part of Blunt Bodies in Hypersonic Flow. WADC Tech. Note 56-294, U.S. Air Force, July 1956.
8. Bertram, M. H., and Baradell, D. L.: A Note on the Sonic-Wedge Leading-Edge Approximation in Hypersonic Flow. Jour. Aero. Sci. (Readers' Forum), vol. 24, no. 8, Aug. 1957, pp. 627-629.
9. Vas, I. E., and Bogdonoff, S. M.: An Exploratory Study at $M = 14$ of the Flow About a Hemisphere Cylinder at Angle of Attack. Rep. No. 438 (WADC TN 58-331, AD 205 461), Dept. Aero. Eng., Princeton Univ., Sept. 1958.
10. Bertram, Mitchel H.: Tip-Bluntness Effects on Cone Pressures at $M = 6.85$. Jour. Aero. Sci. (Readers' Forum), vol. 23, no. 9, Sept. 1956, pp. 898-900.

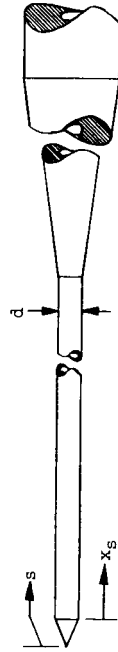
11. Vas, I. E., and Bogdonoff, S. M.: Hypersonic Studies of Blunt Unswept Wings. Rep. No. 450 (WADC TN 59-127, AD 214 623), Dept. Aero. Eng., Princeton Univ., Apr. 1959.
12. Baradell, Donald L.: Experimental Verification of Boundary-Layer Corrections in Hypersonic Nozzles. Jour. Aero/Space Sci. (Readers' Forum), vol. 26, no. 7, July 1959, pp. 454-455.
13. Love, Eugene S., Coletti, Donald E., and Bromm, August F., Jr.: Investigation of the Variation With Reynolds Number of the Base, Wave, and Skin-Friction Drag of a Parabolic Body of Revolution (NACA RM-10) at Mach Numbers of 1.62, 1.93, and 2.41 in the Langley 9-Inch Supersonic Tunnel. NACA RM L52H21, 1952.
14. Love, E. S.: Generalized-Newtonian Theory. Jour. Aero/Space Sci. (Readers' Forum), vol. 26, no. 5, May 1959, pp. 314-315.
15. Sakurai, Akira: On the Propagation and Structure of the Blast Wave, I. Jour. Phys. Soc. of Japan, vol. 8, no. 5, Sept.-Oct. 1953, pp. 662-669.
16. Sakurai, Akira: On the Propagation and Structure of a Blast Wave, II. Jour. Phys. Soc. of Japan, vol. 9, no. 2, Mar.-Apr. 1954, pp. 256-266.
17. Taylor, Geoffrey: The Formation of a Blast Wave by a Very Intense Explosion. Proc. Roy. Soc. (London), ser. A, vol. 201, no. 1065, Mar. 22, 1950.
I. Theoretical Discussion, pp. 159-174.
II. The Atomic Explosion of 1945, pp. 175-186.
18. Lin, Shao-Chi: Cylindrical Shock Waves Produced by Instantaneous Energy Release. Jour. Appl. Phys., vol. 25, no. 1, Jan. 1954, pp. 54-57.
19. Cheng, H. K., and Pallone, A. J.: Inviscid Leading-Edge Effect in Hypersonic Flow. Jour. Aero. Sci. (Readers' Forum), vol. 23, no. 7, July 1956, pp. 700-702.
20. Love, E. S.: Prediction of Inviscid Induced Pressures From Round Leading Edge Blunting at Hypersonic Speeds. ARS Jour. (Tech. Notes), vol. 29, no. 10, pt. 1, Oct. 1959, pp. 792-794.
21. Casaccio, Anthony: Theoretical Pressure Distribution on a Hemisphere-Cylinder Combination. Jour. Aero/Space Sci. (Readers' Forum), vol. 26, no. 1, Jan. 1959, pp. 63-64.

22. Wagner, Richard D., Jr.: Some Aspects of the Modified Newtonian and Prandtl-Meyer-Expansion Method for Axisymmetric Blunt Bodies at Zero Angle of Attack. Jour. Aero/Space Sci. (Readers' Forum), vol. 26, no. 12, Dec. 1959, pp. 851-852.

TABLE I.- LOCATION OF ORIFICES ON BASIC TEST MODELS

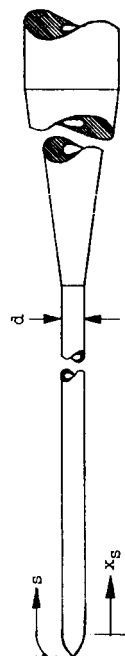
[Orifice diameter, 0.030 inch; $d = 0.090$ inch](a) 90° cone

Orifice	Location			Location		
	x_s , in.	s , in.	x_s/d	x_s/d	s/d	s/d
1	0.0313	0.0945	0.3478	0.3478	1.0500	1.0500
2	0.1250	0.1882	1.3889	1.3889	2.0911	2.0911
3	0.2500	0.3132	2.7778	2.7778	3.4800	3.4800
4	0.5000	0.5632	5.5556	5.5556	6.2578	6.2578
5	1.0000	1.0632	11.1111	11.1111	11.8133	11.8133
6	1.5000	1.5632	16.6667	16.6667	17.3689	17.3689
7	2.0000	2.0632	22.2222	22.2222	22.9244	22.9244
8	2.5000	2.5632	27.7778	27.7778	28.4800	28.4800
9	3.0000	3.0632	33.3333	33.3333	34.0356	34.0356
10	3.5000	3.5632	38.8889	38.8889	39.5911	39.5911
11	4.0000	4.0632	44.4444	44.4444	45.1467	45.1467
12	4.5000	4.5632	50.0000	50.0000	50.7022	50.7022

(b) 45° cone

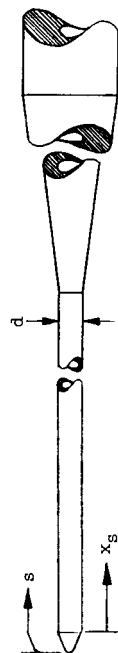
Orifice	Location			Location		
	x_s , in.	s , in.	x_s/d	x_s/d	s/d	s/d
1	0.0313	0.1489	0.3478	0.3478	1.6544	1.6544
2	0.1250	0.2426	1.3889	1.3889	2.6956	2.6956
3	0.2500	0.3676	2.7778	2.7778	4.0844	4.0844
4	0.5000	0.6176	5.5556	5.5556	6.8622	6.8622
5	1.0000	1.1176	11.1111	11.1111	12.4178	12.4178
6	1.5000	1.6176	16.6667	16.6667	17.9733	17.9733
7	2.0000	2.1176	22.2222	22.2222	23.5289	23.5289
8	2.5000	2.6176	27.7778	27.7778	29.0844	29.0844
9	3.0000	3.1176	33.3333	33.3333	34.6400	34.6400
10	3.5000	3.6176	38.8889	38.8889	40.1956	40.1956
11	4.0000	4.1176	44.4444	44.4444	45.7511	45.7511
12	4.5000	4.6176	50.0000	50.0000	51.3067	51.3067

TABLE I.- LOCATION OF ORIFICES ON BASIC TEST MODELS - Continued



(c) Modified hemisphere (90° conical tip)

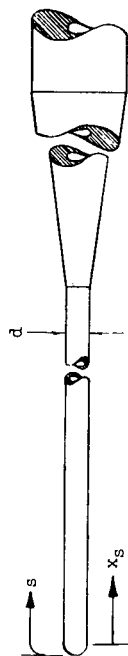
Orifice	Location			Location	
	x_s , in.	s , in.	x_s/d	s/d	
1	0.0313	0.1116	0.3478	1.239	
2	0.1250	0.2053	1.3889	2.275	
3	0.2500	0.3303	2.7778	3.665	
4	0.5000	0.5803	5.5556	6.448	
5	1.0000	1.0803	11.1111	12.010	
6	1.5000	1.5803	16.6667	17.525	
7	2.0000	2.0803	22.2222	23.095	
8	2.5000	2.5803	27.7778	28.650	
9	3.0000	3.0803	33.3333	34.200	
10	3.5000	3.5803	38.8889	39.720	
11	4.0000	4.0803	44.4444	45.220	
12	4.5000	4.5803	50.0000	50.810	



(d) 45° blunt cone

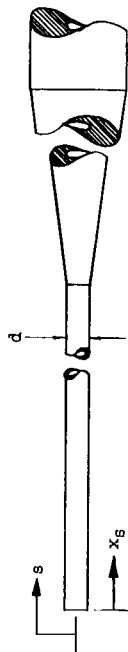
Orifice	Location			Location	
	x_s , in.	s , in.	x_s/d	s/d	
1	0.0313	0.1210	0.3478	1.3444	
2	0.1250	0.2147	1.3889	2.3856	
3	0.2500	0.3397	2.7778	3.7744	
4	0.5000	0.5897	5.5556	6.5222	
5	1.0000	1.0897	11.1111	12.1078	
6	1.5000	1.5897	16.6667	17.6633	
7	2.0000	2.0897	22.2222	23.2189	
8	2.5000	2.5897	27.7778	28.7744	
9	3.0000	3.0897	33.3333	34.3300	
10	3.5000	3.5897	38.8889	39.8856	
11	4.0000	4.0897	44.4444	45.4411	
12	4.5000	4.5897	50.0000	50.9967	

TABLE I.- LOCATION OF ORIFICES ON BASIC TEST MODELS - Concluded



(e) Hemisphere

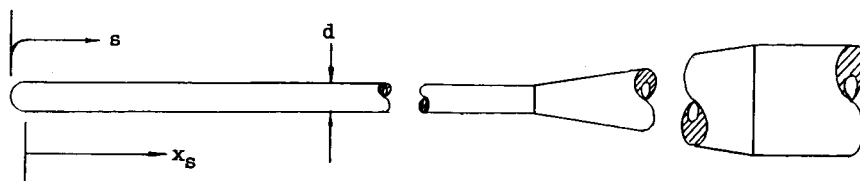
Orifice	Location			Location		
	x_s , in.	s , in.	x_s/d	s/d	s/d	s/d
1	0.0313	0.1020	0.3478	1.1333	1.1333	1.1333
2	0.1250	0.1957	1.3889	2.1744	2.1744	2.1744
3	0.2500	0.3207	2.7778	3.5633	3.5633	3.5633
4	0.5000	0.5707	5.5556	6.3411	6.3411	6.3411
5	1.0000	1.0707	11.1111	11.8967	11.8967	11.8967
6	1.5000	1.5707	16.6667	17.4522	17.4522	17.4522
7	2.0000	2.0707	22.2222	23.0078	23.0078	23.0078
8	2.5000	2.5707	27.7778	28.5633	28.5633	28.5633
9	3.0000	3.0707	33.3333	34.1189	34.1189	34.1189
10	3.5000	3.5707	38.8889	39.6744	39.6744	39.6744
11	4.0000	4.0707	44.4444	45.2300	45.2300	45.2300
12	4.5000	4.5707	50.0000	50.7856	50.7856	50.7856



(f) Flat face

Orifice	Location			Location		
	x_s , in.	s , in.	x_s/d	s/d	s/d	s/d
1	0.0313	0.0763	0.3478	0.8478	0.8478	0.8478
2	0.1250	0.1700	1.3889	1.8889	1.8889	1.8889
3	0.2500	0.2950	2.7778	3.2778	3.2778	3.2778
4	0.5000	0.5450	5.5556	6.0556	6.0556	6.0556
5	1.0000	1.0450	11.1111	11.6111	11.6111	11.6111
6	1.5000	1.5450	16.6667	17.1667	17.1667	17.1667
7	2.0000	2.0450	22.2222	22.7222	22.7222	22.7222
8	2.5000	2.5450	27.7778	28.2778	28.2778	28.2778
9	3.0000	3.0450	33.3333	33.8333	33.8333	33.8333
10	3.5000	3.5450	38.8889	39.3889	39.3889	39.3889
11	4.0000	4.0450	44.4444	44.9444	44.9444	44.9444
12	4.5000	4.5450	50.0000	50.5000	50.5000	50.5000

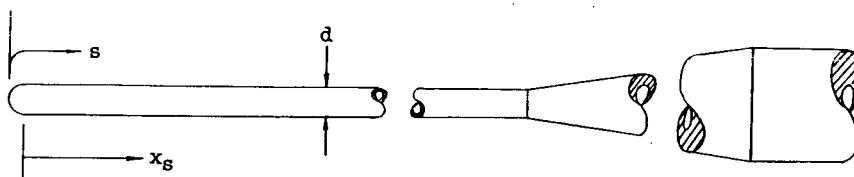
TABLE II.- LOCATION OF ORIFICES ON 11-INCH HYPERSONIC TUNNEL MODELS



(a) 1-inch-diameter model

[Diameter of orifices 1 to 5, 0.090 inch;
diameter of orifices 6 to 16, 0.063 inch]

Orifice	Location		Location	
	x_s , in.	s , in.	x_s/d	s/d
1	---	0	---	0
2	---	0.3927	---	0.3927
3	0	0.7854	0	0.7854
4	0.5	1.2854	0.5	1.2854
5	1.0	1.7854	1.0	1.7854
6	1.5	2.2854	1.5	2.2854
7	2.0	2.7854	2.0	2.7854
8	2.5	3.2854	2.5	3.2854
9	3.0	3.7854	3.0	3.7854
10	3.5	4.2854	3.5	4.2854
11	4.0	4.7854	4.0	4.7854
12	4.5	5.2854	4.5	5.2854
13	5.5	6.284	5.5	6.2854
14	6.5	7.2854	6.5	7.2854
15	7.5	8.2854	7.5	8.2854
16	8.5	9.2854	8.5	9.2854



(b) 3/8-inch-diameter model

[Orifice diameter, 0.063 inch]

Orifice	Location		Location	
	x_s , in.	s , in.	x_s/d	s/d
1	1.0313	1.3258	2.75	3.5355
2	2.0625	2.3570	5.5	6.2853
3	3.3750	3.6695	9.0	9.7853

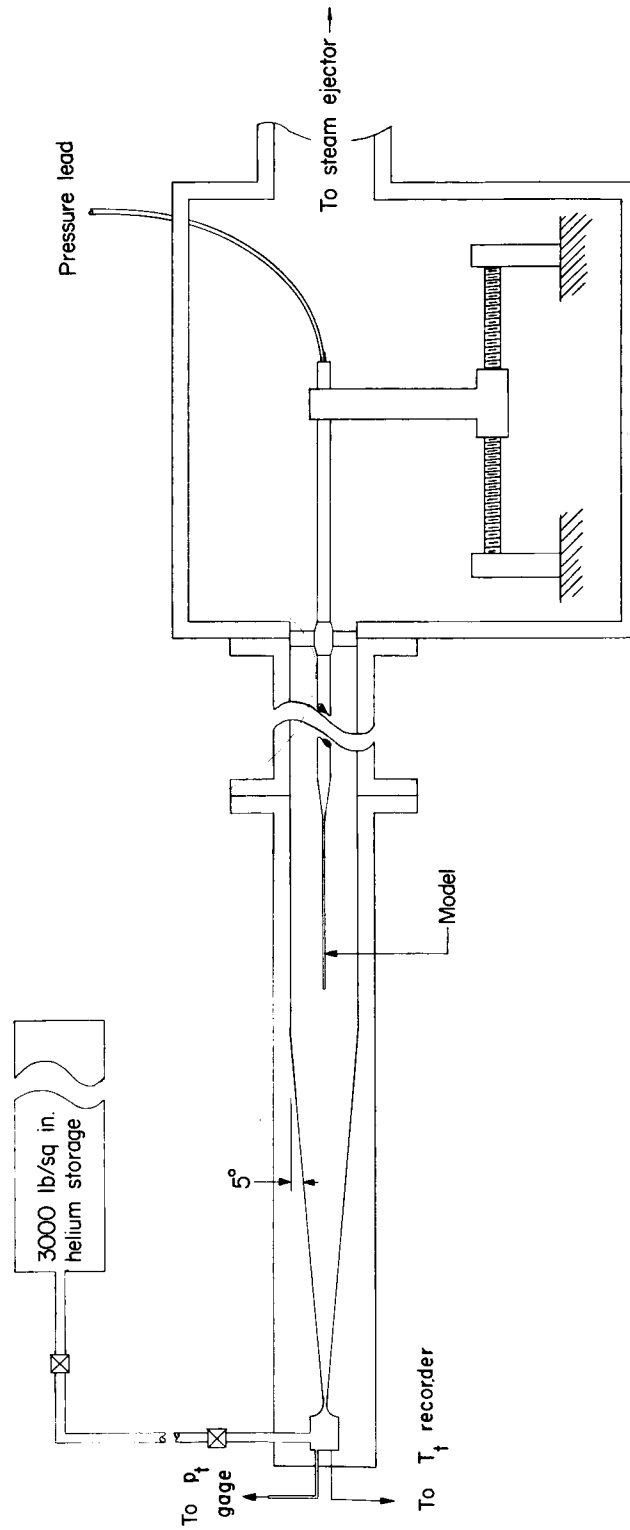
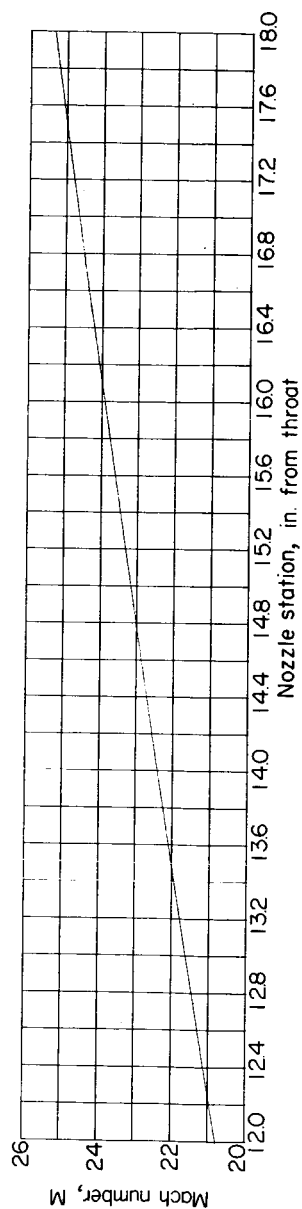
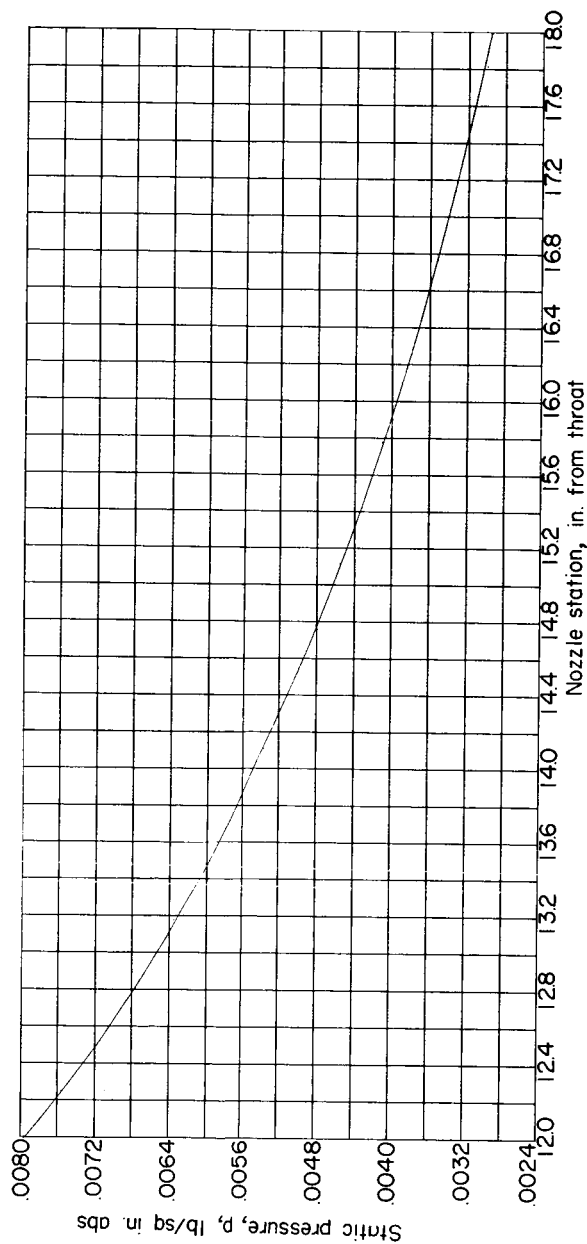


Figure 1.- Schematic diagram of operating circuit of a 2-inch helium tunnel at the Langley Research Center.

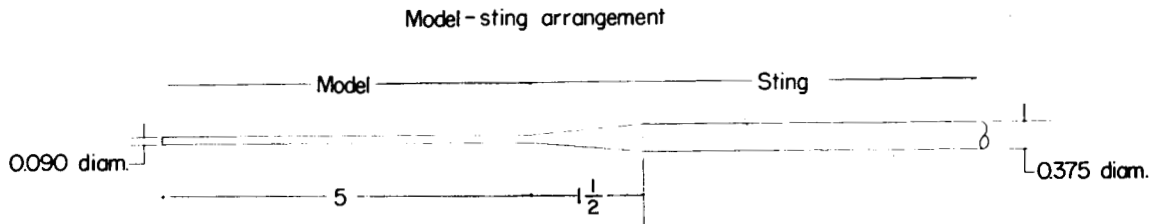


(a) Mach number distribution.



(b) Static-pressure distribution.

Figure 2.- Mach number and static-pressure distribution along 2-inch helium nozzle axis.
 $P_t = 2,015$ lb/sq in. abs.



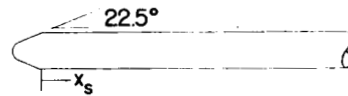
Nose shapes



(a) 90° cone.



(b) 45° cone.

(c) Modified hemisphere,
90° conical tip.(d) 45° blunt cone,
diameter of nose = $1/2d$.

(e) Hemisphere.



(f) Flat.

Figure 3.- Dimensional details of model-sting arrangement and description of nose shapes employed in this investigation. (All dimensions are in inches.)

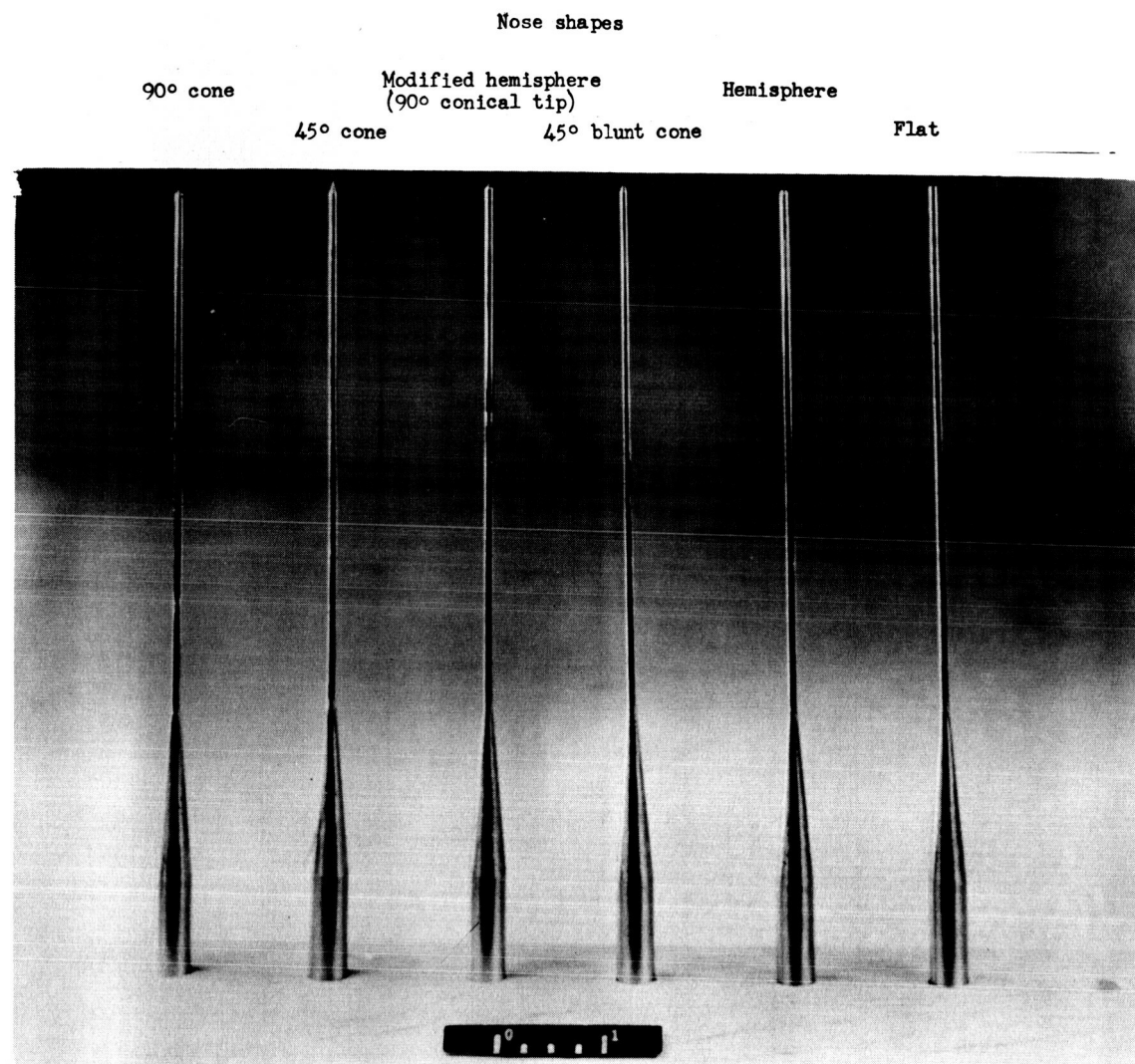


Figure 4.- Basic test models.

L-58-4043.1

I-848

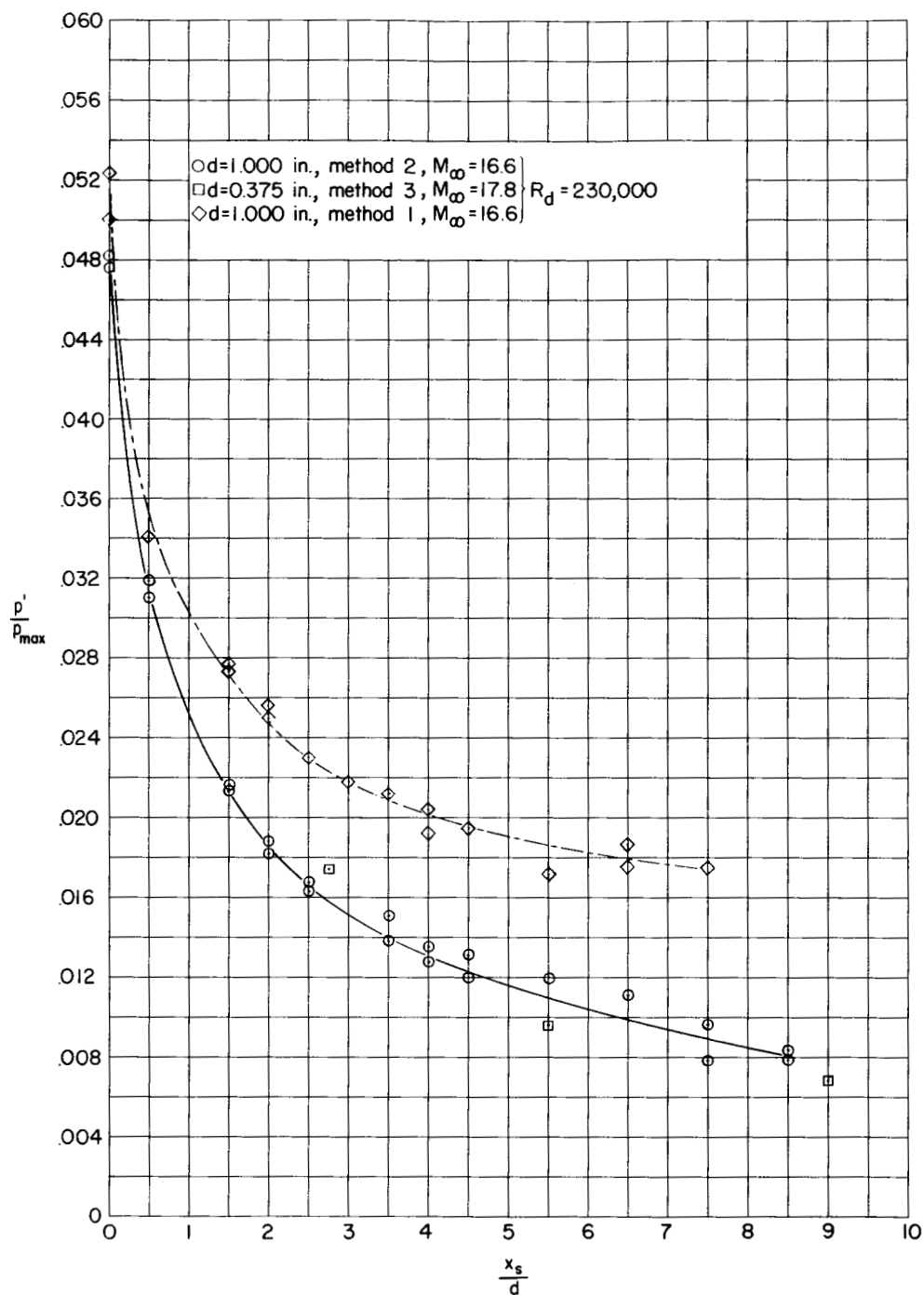


Figure 5.- Variation of induced pressures on a hemisphere-cylinder model in the Langley 11-inch hypersonic tunnel, showing the effects of out-gassing on test results.

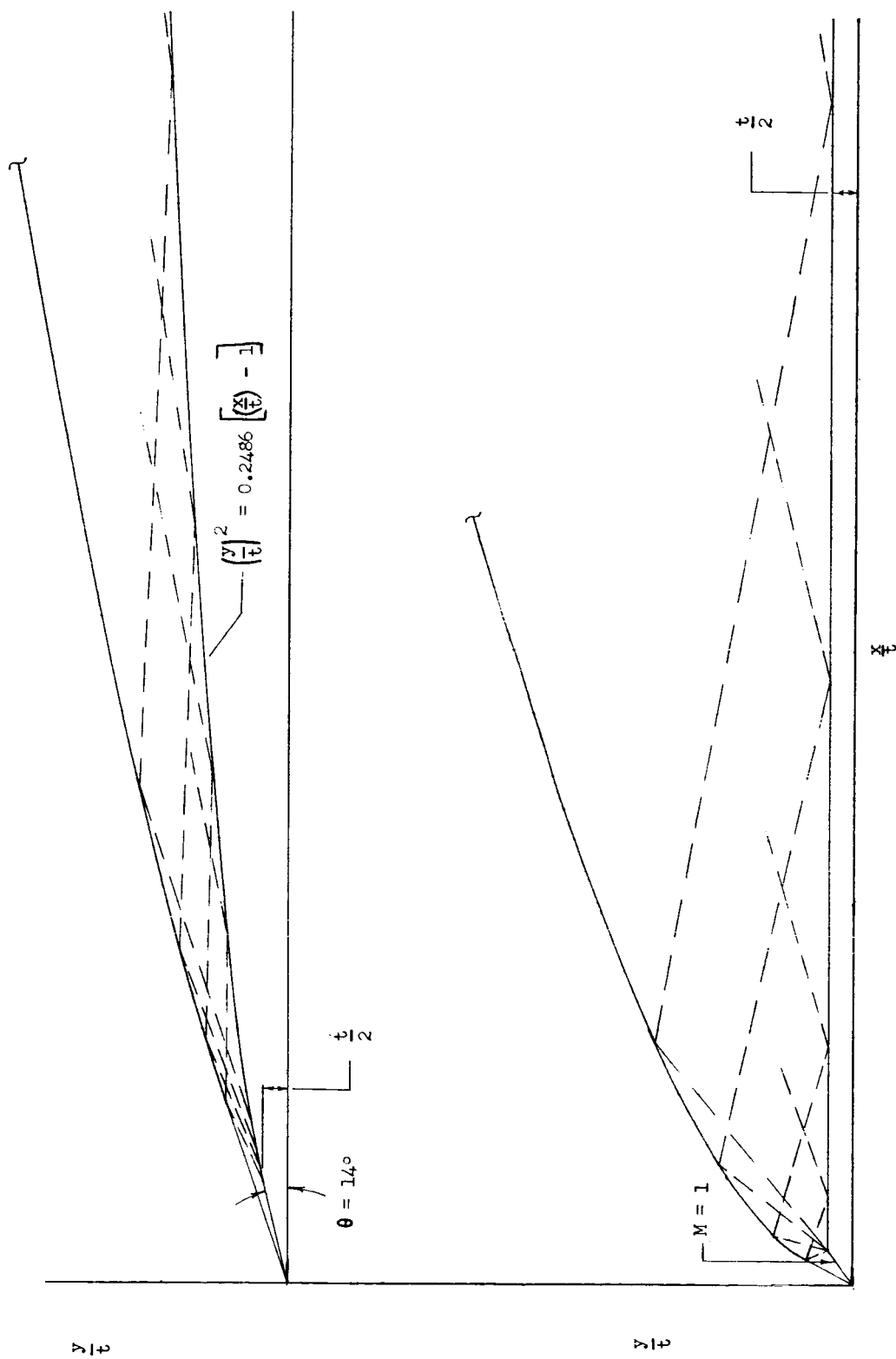


Figure 6.- Shock shape and illustrative characteristics network on sharp and blunt shapes at $M_{\infty, n} = 25$. $\gamma = 5/3$.

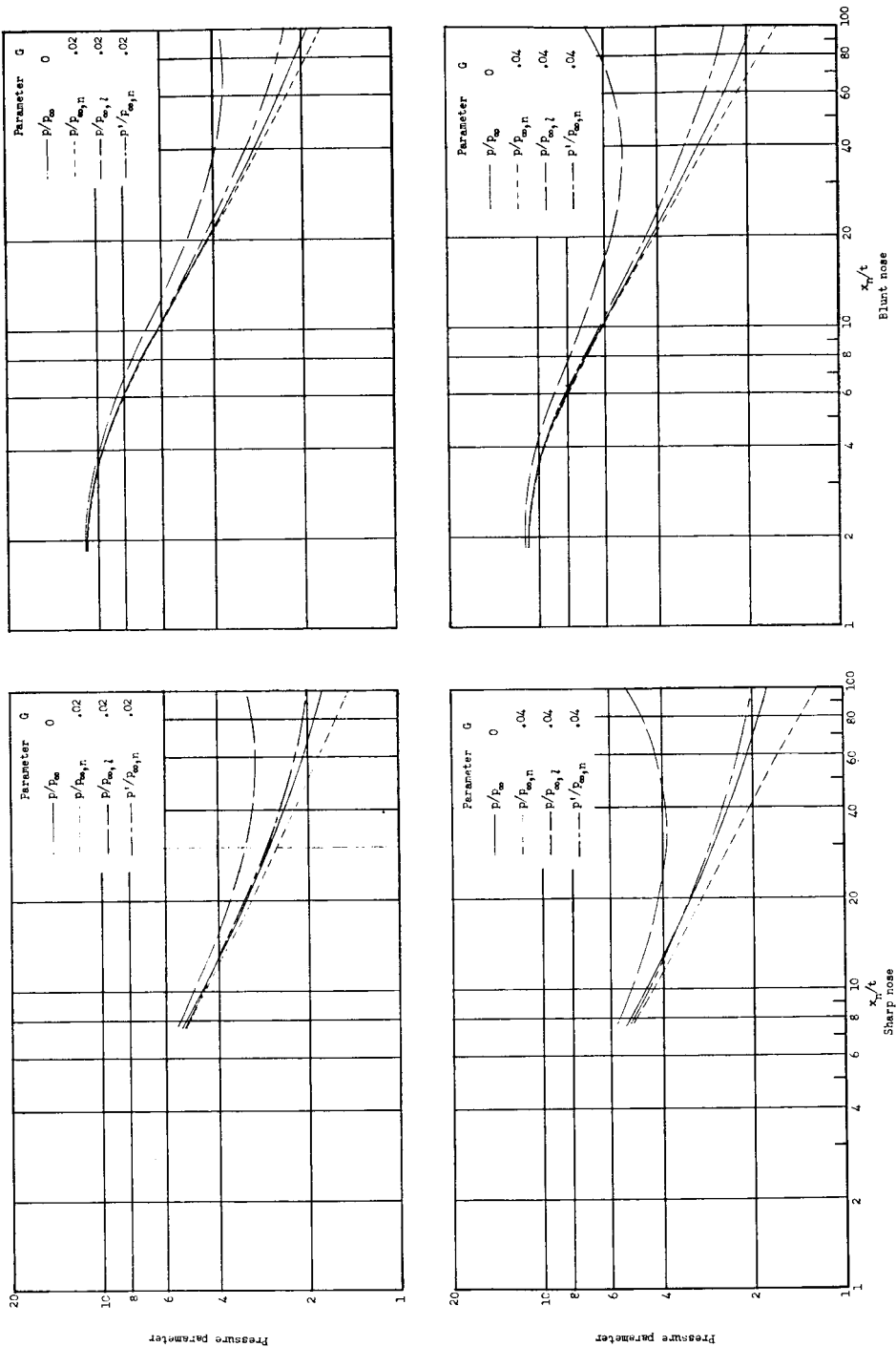
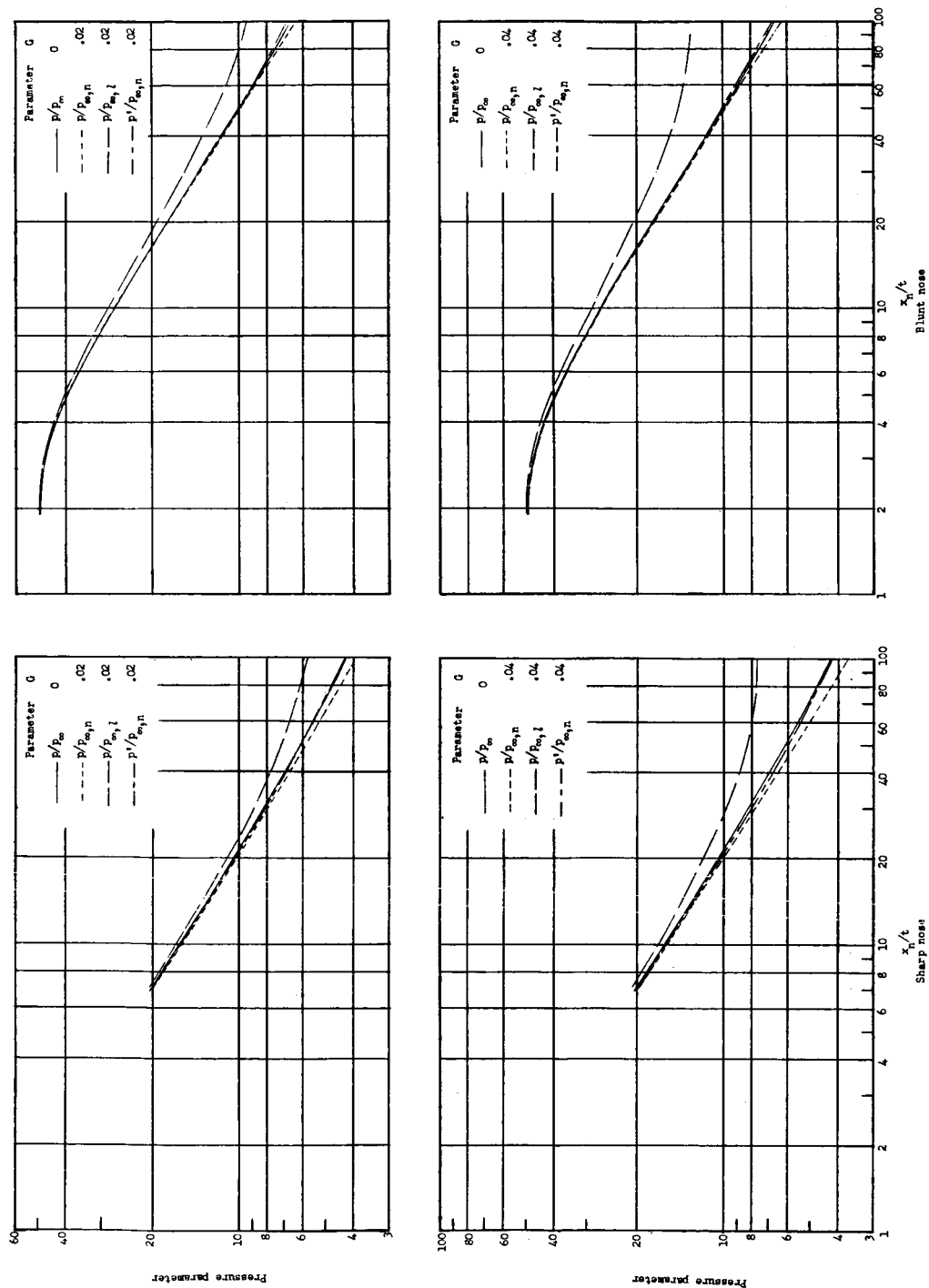
(a) $M_{\infty,n} = 11.5$.

Figure 7.- Effect of pressure reduction method on pressures obtained on sharp-nose and blunt-nose two-dimensional shapes in linearly varying Mach number flow, and comparison with pressures on same shapes in constant Mach number flow.



(b) $M_{\infty,n} = 25$.

Figure 7.- Concluded.

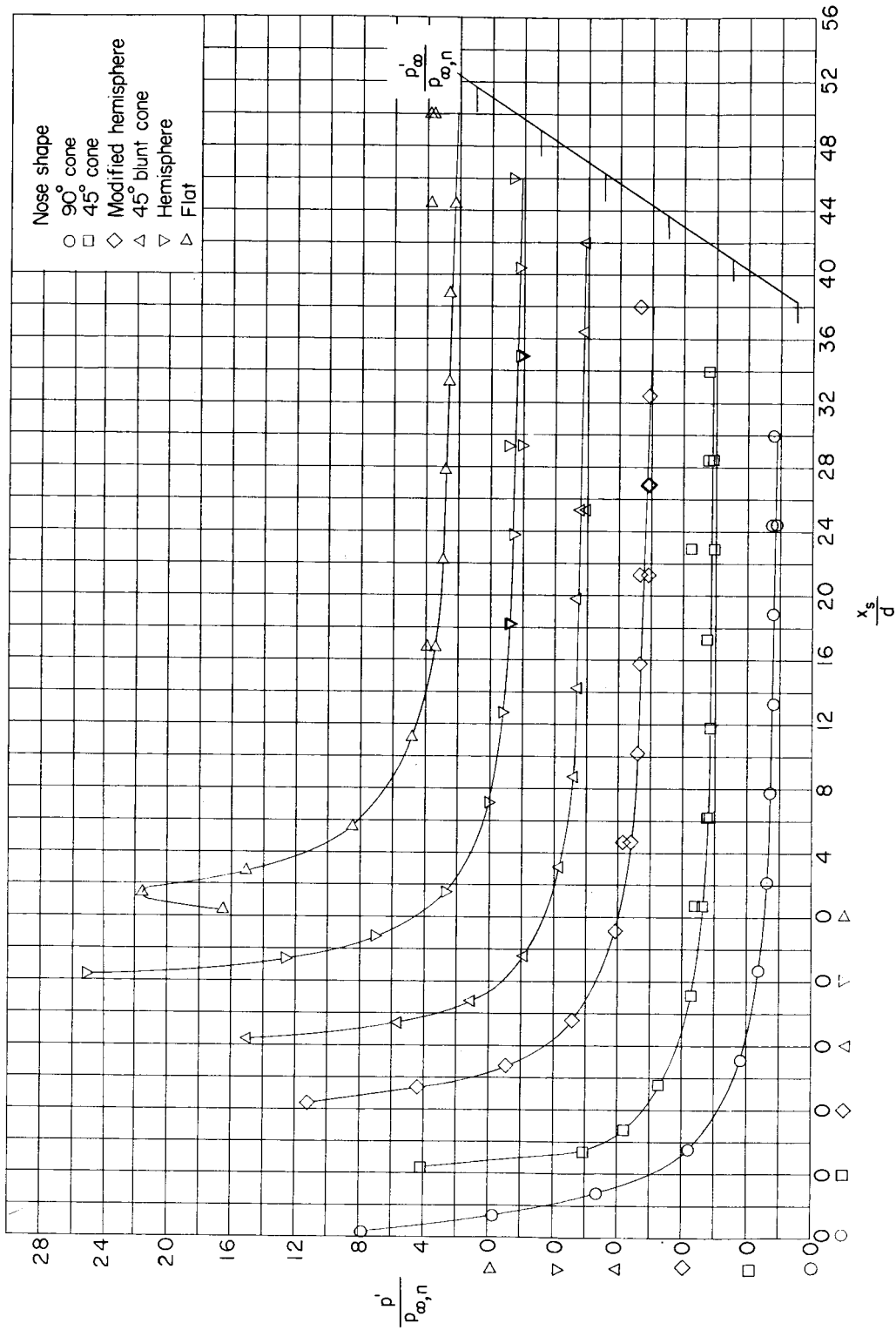
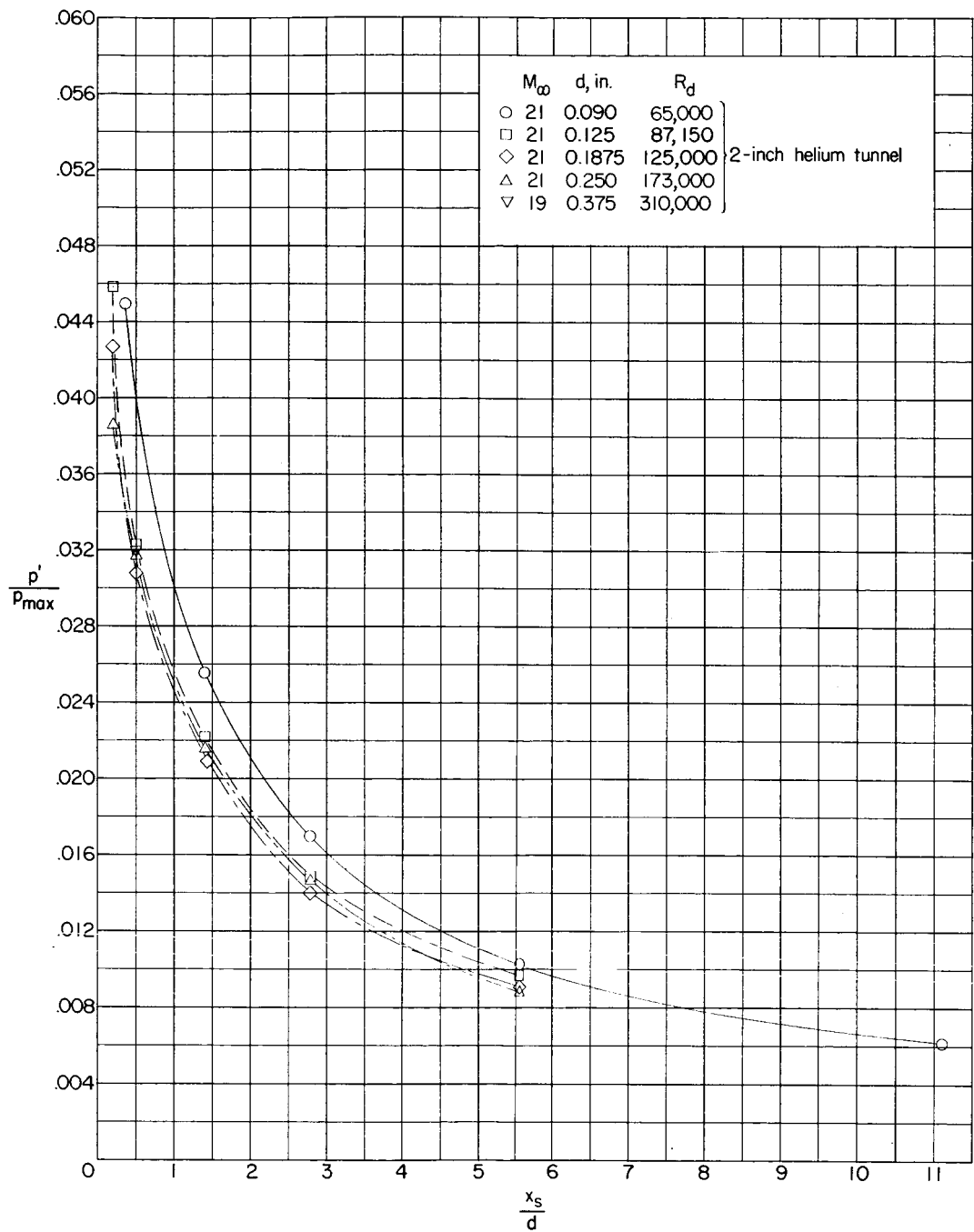


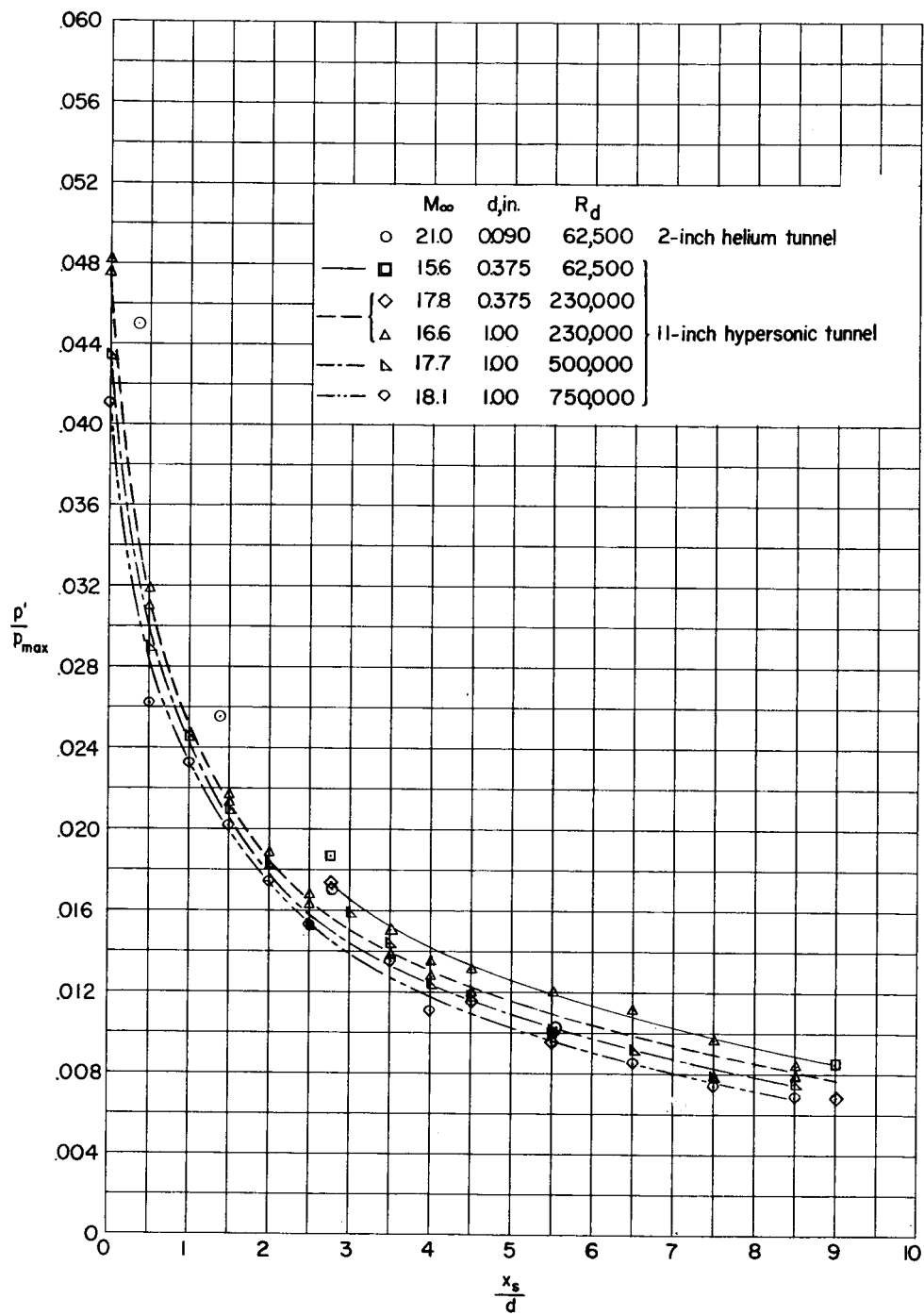
Figure 8.- Variation of induced pressures on basic test models. $M_{\infty} = 21$.

L-848



(a) A 2-inch helium tunnel at the Langley Research Center.

Figure 9.- Effect of Reynolds number on measured induced pressures on hemisphere models.



(b) Langley 11-inch hypersonic tunnel.

Figure 9.- Concluded.

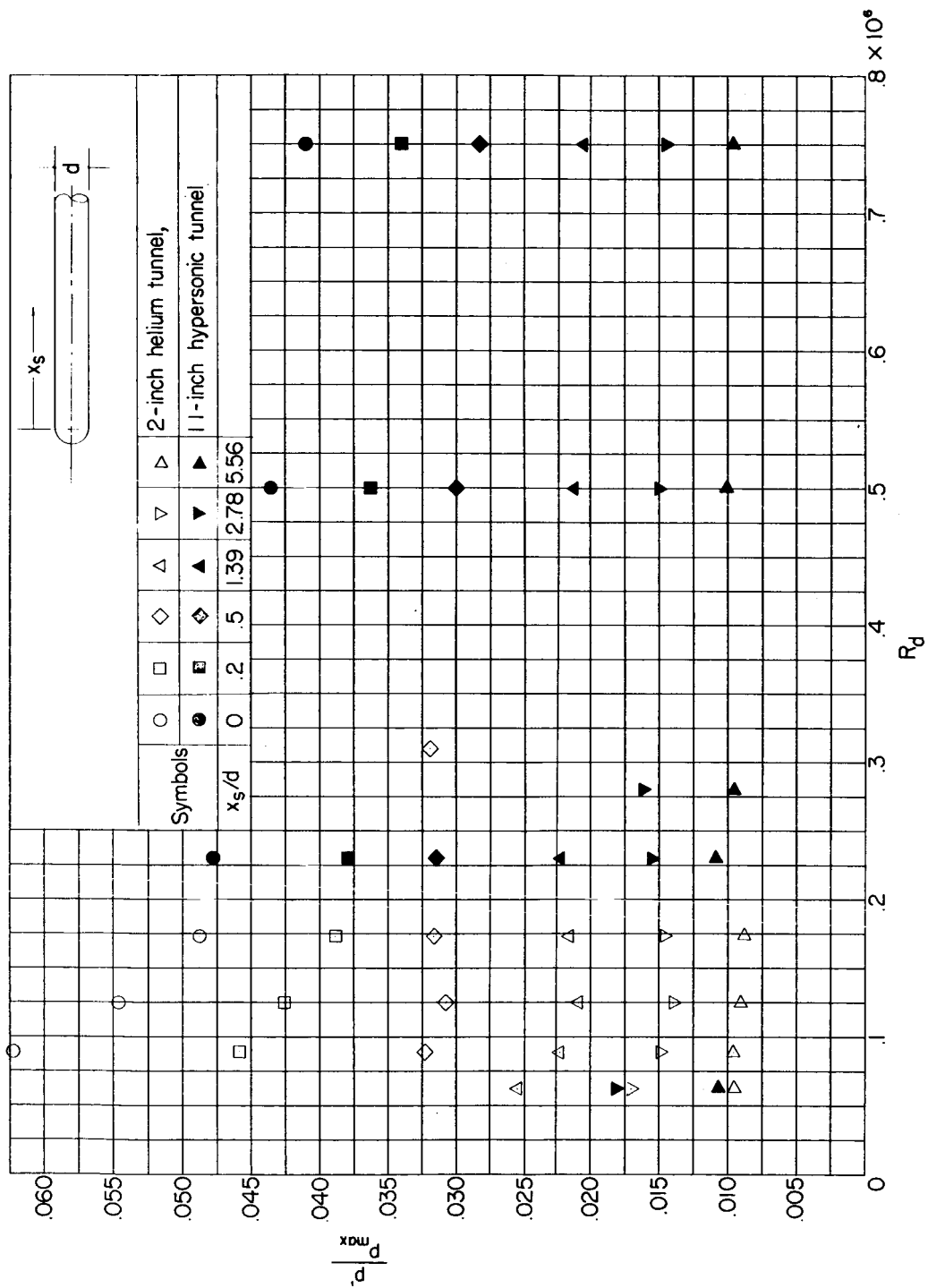


Figure 10.- Summary plot showing the effects of Reynolds number on the induced pressures measured on hemisphere cylinders.

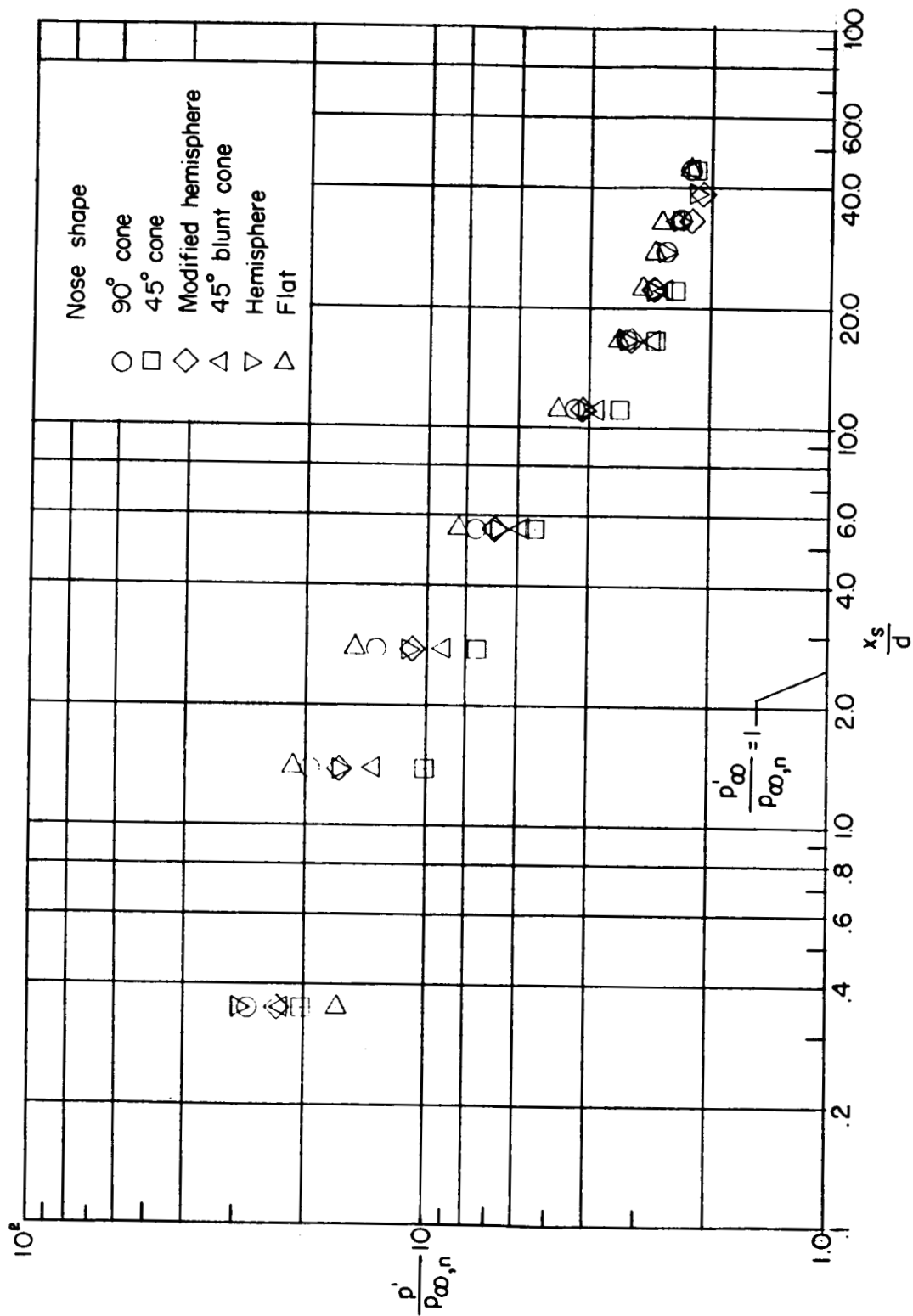


Figure 11.- Effects of nose shape on induced pressures.

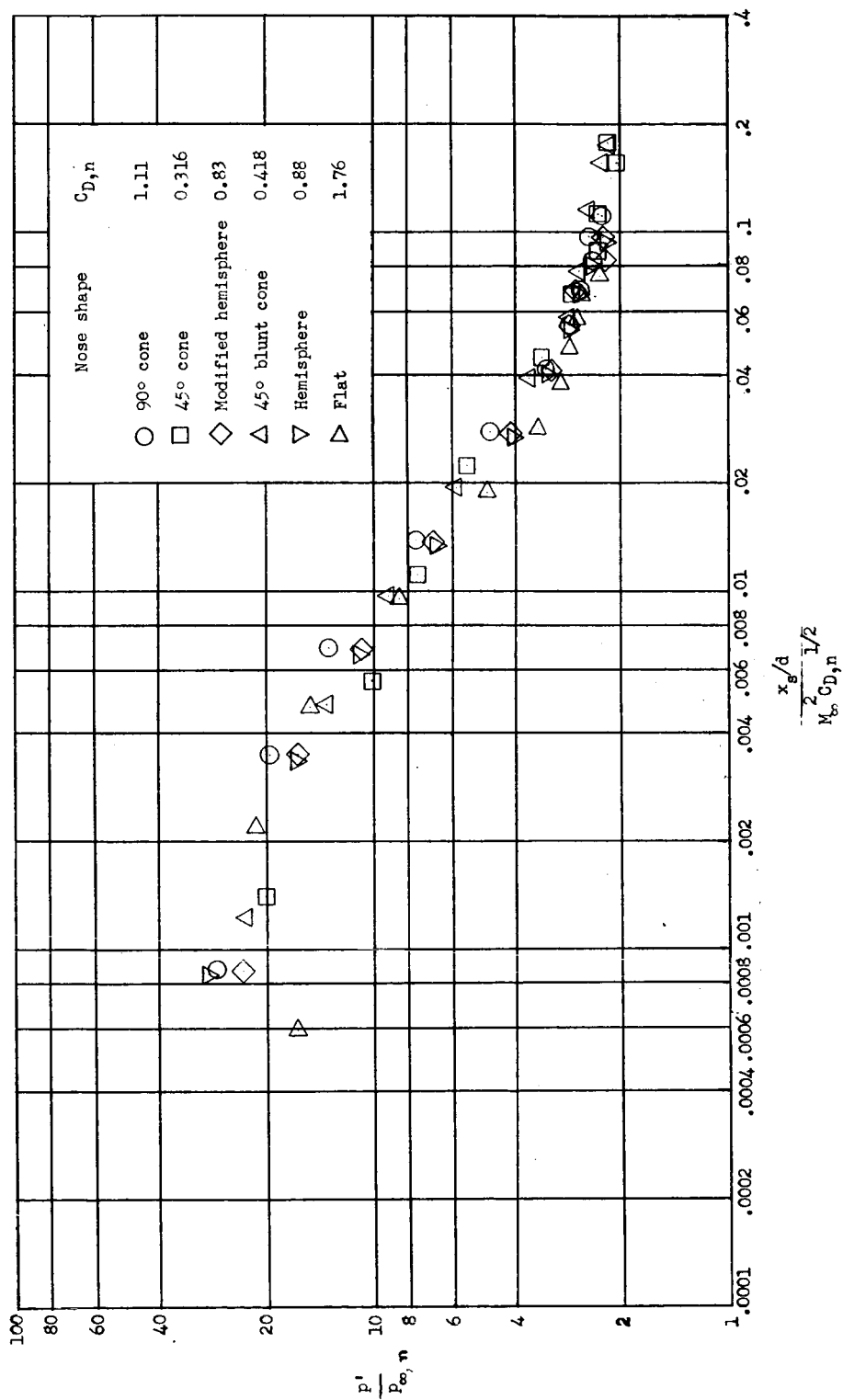


Figure 12.- Correlation of the measured induced pressures on the basic test models on the basis of blast-wave-theory parameters.

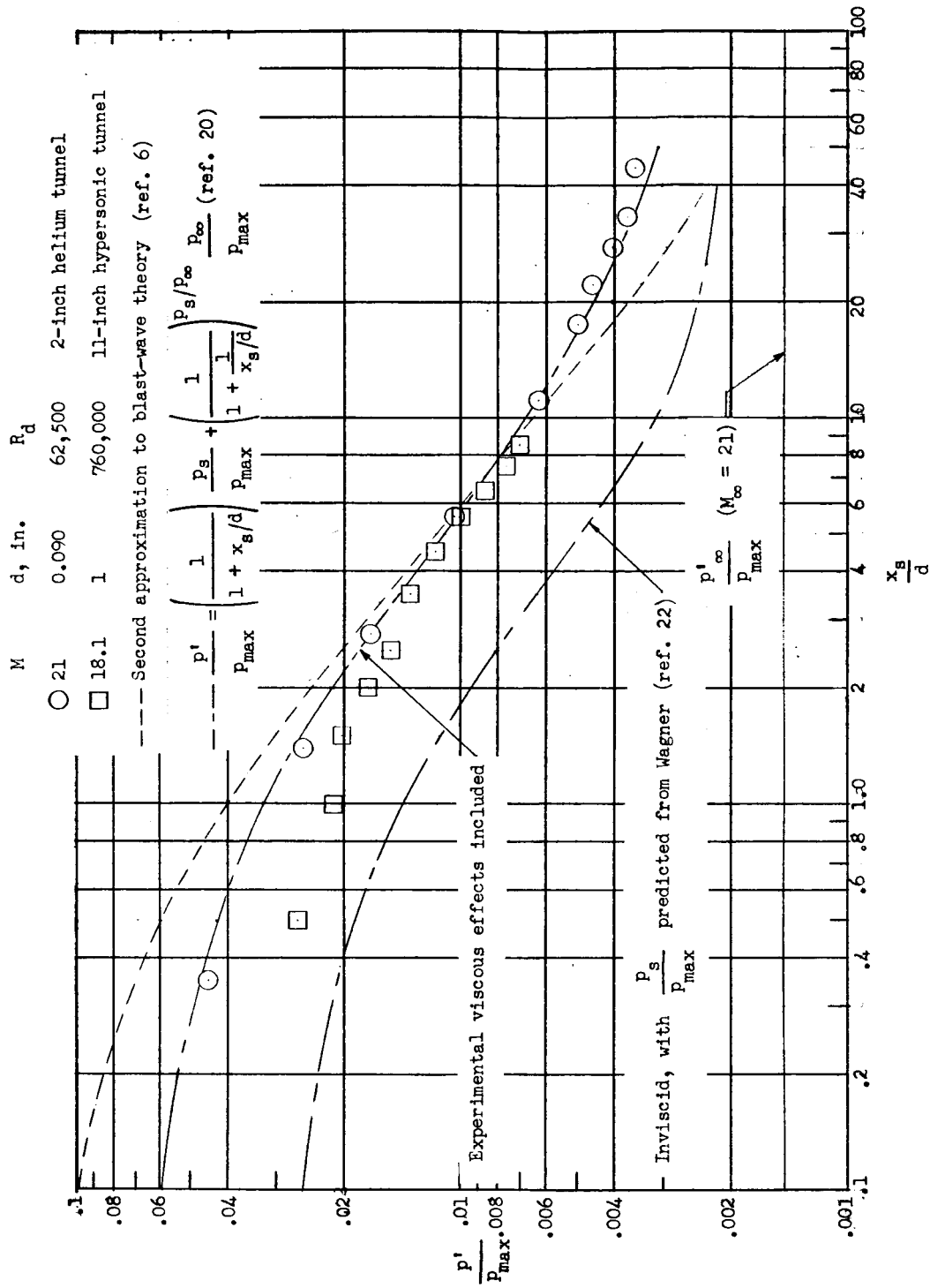


Figure 13.- Comparison of experimentally obtained induced pressures on hemisphere-cylinder models with blast-wave theory and a modified blast-wave theory.

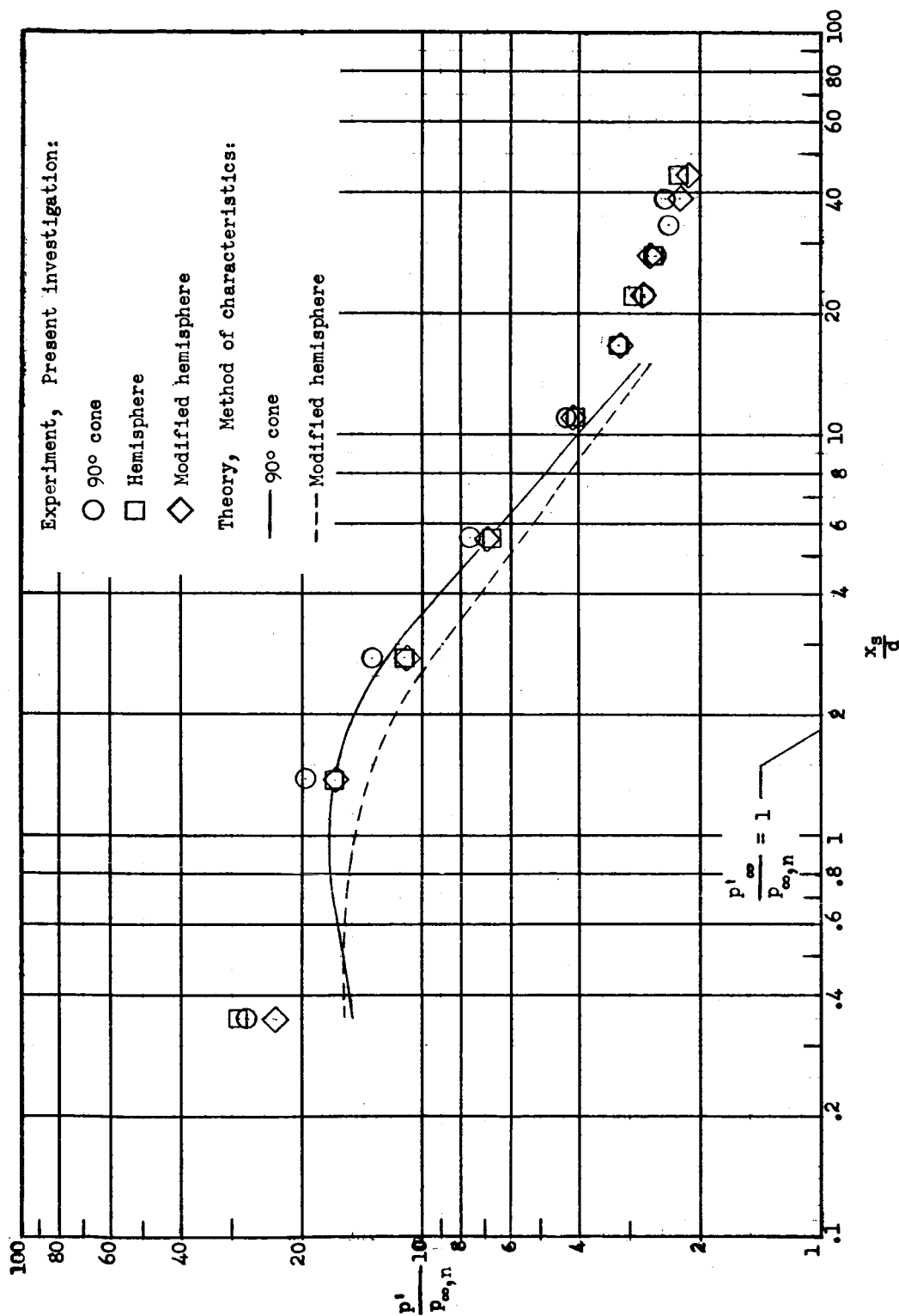
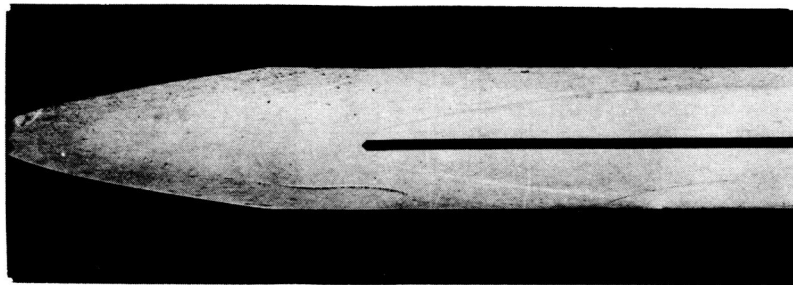
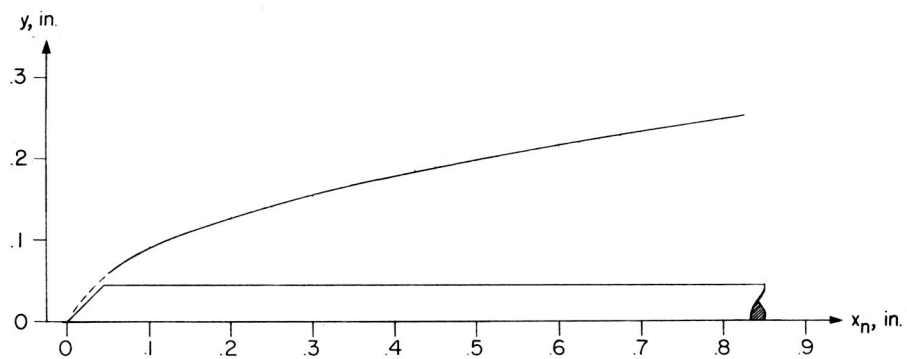


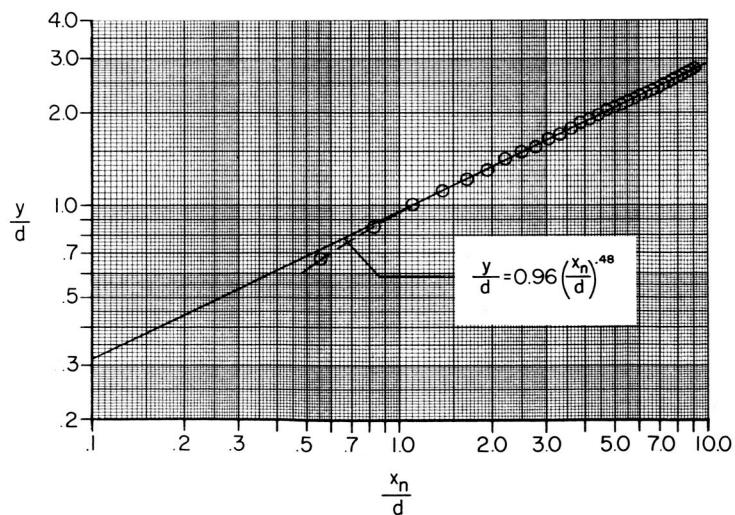
Figure 14.- Comparison of experimental induced pressures with those calculated by the method of characteristics.



(a) Schlieren photograph of model. L-60-249

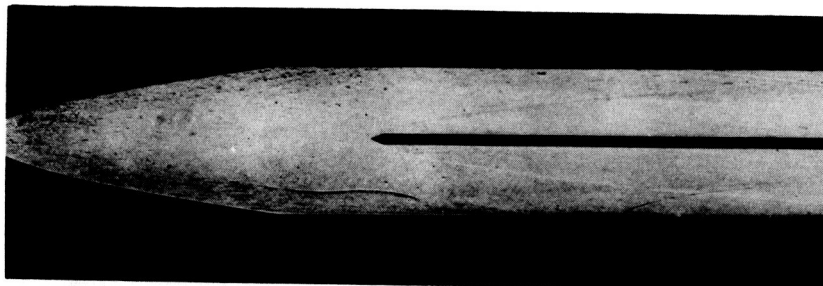


(b) Shock-wave shape.

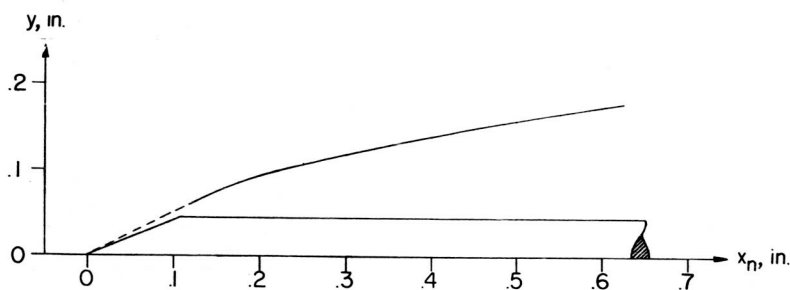


(c) Shock-wave coordinates.

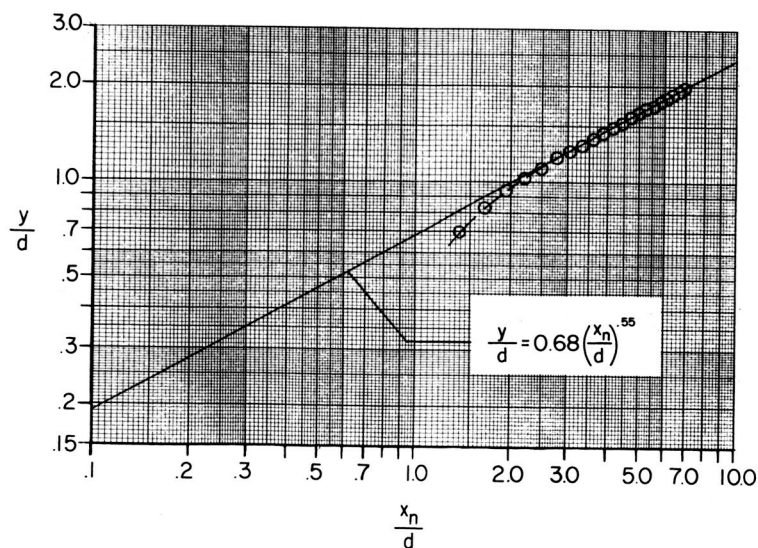
Figure 15.- Shock-shape characteristics on the 90° cone.
 $d = 0.090$ inch; $M_\infty = 21$.



(a) Schlieren photograph of model. L-60-250

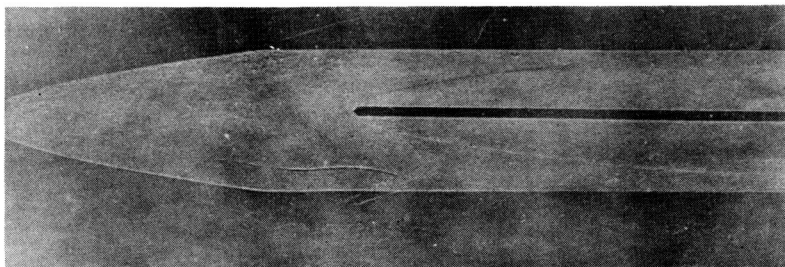


(b) Shock-wave shape.

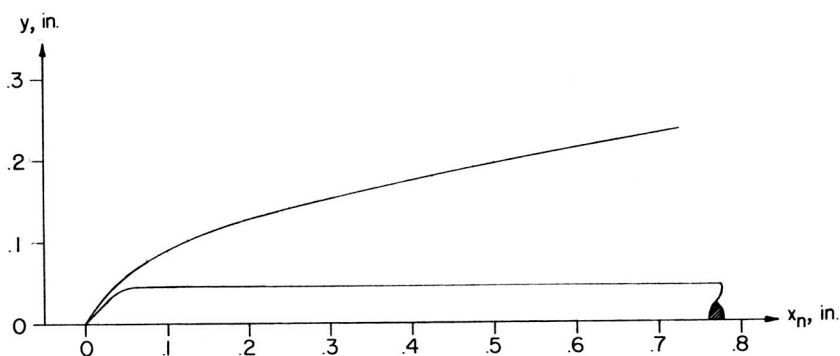


(c) Shock-wave coordinates.

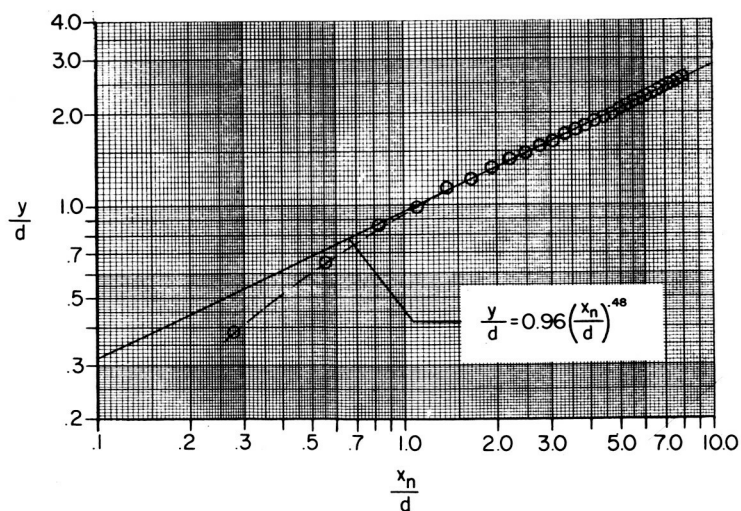
Figure 16.- Shock-shape characteristics on the 45° cone.
 $d = 0.090$ inch; $M_\infty = 21$.



(a) Schlieren photograph of model. L-60-251

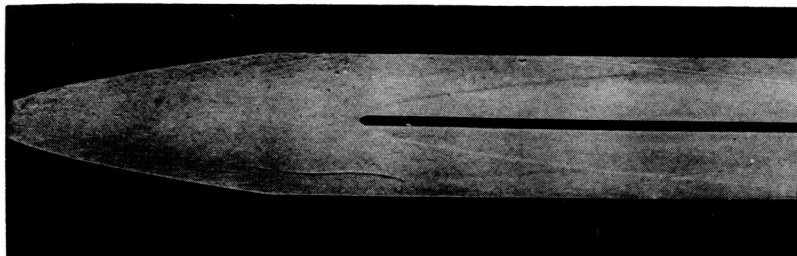


(b) Shock-wave shape.

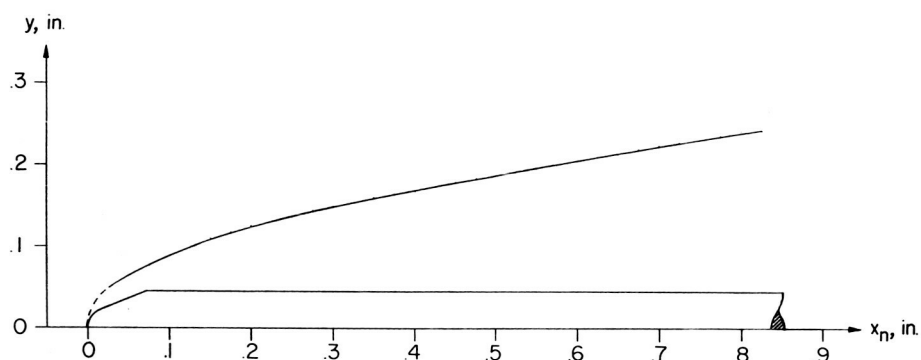


(c) Shock-wave coordinates.

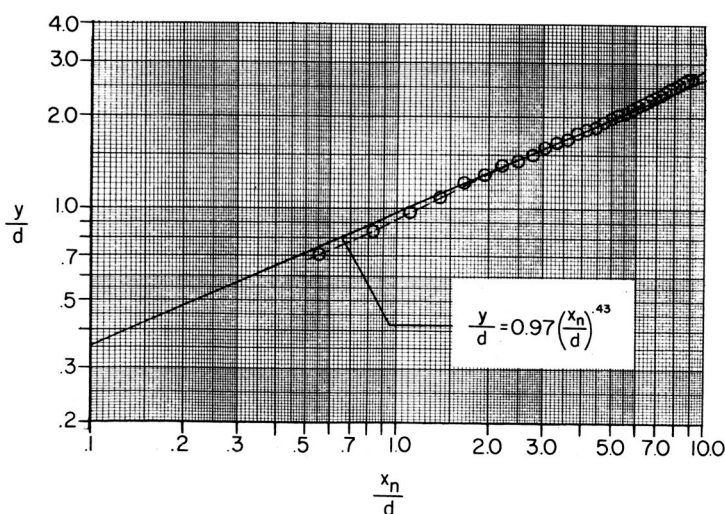
Figure 17.- Shock-shape characteristics on the modified hemisphere.
 $d = 0.090 \text{ inch}$; $M_\infty = 21$.



(a) Schlieren photograph of model. L-60-252

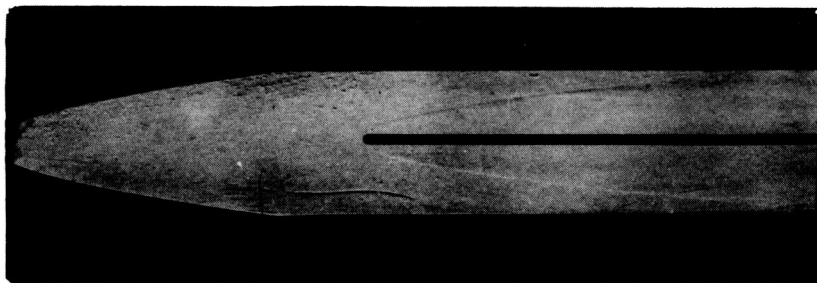


(b) Shock-wave shape.

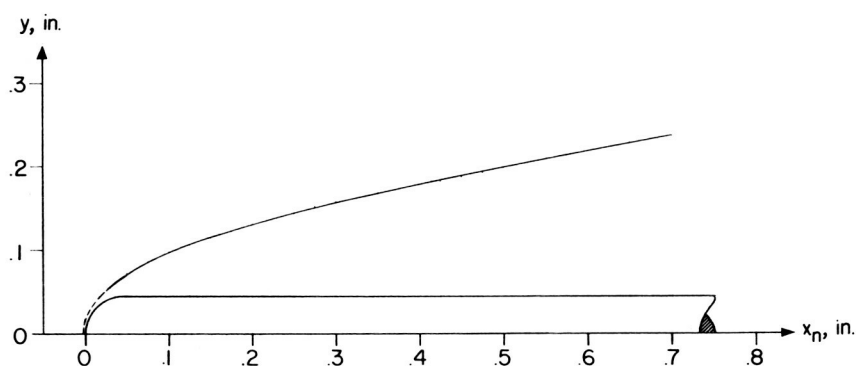


(c) Shock-wave coordinates.

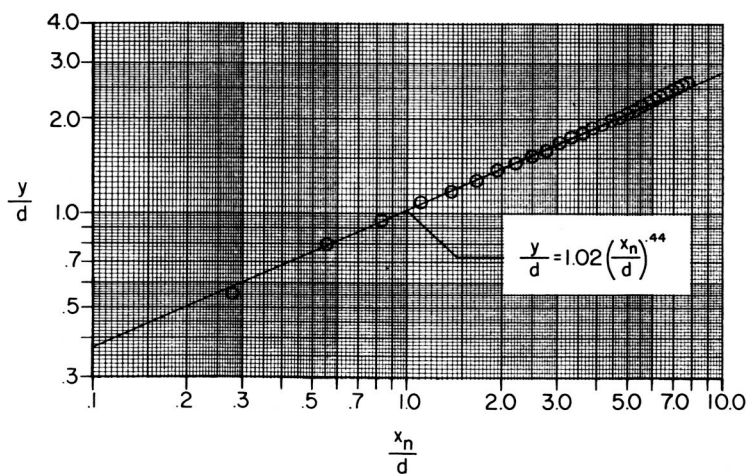
Figure 18.- Shock-shape characteristics on the 45° blunt cone.
 $d = 0.090$ inch; $M_\infty = 21$.



(a) Schlieren photograph of model. L-60-253

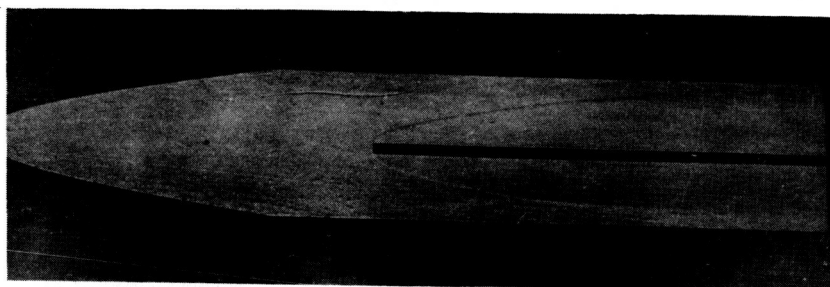


(b) Shock-wave shape.

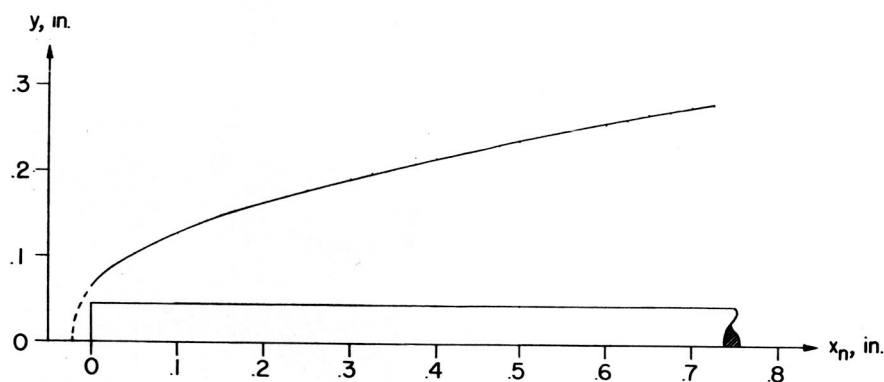


(c) Shock-wave coordinates.

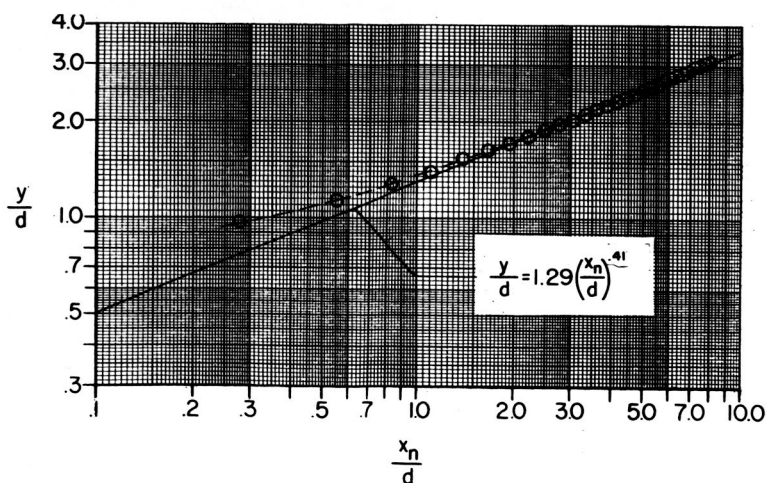
Figure 19.- Shock-shape characteristics on the hemisphere.
 $d = 0.090$ inch; $M_\infty = 21$.



(a) Schlieren photograph of model. L-60-254

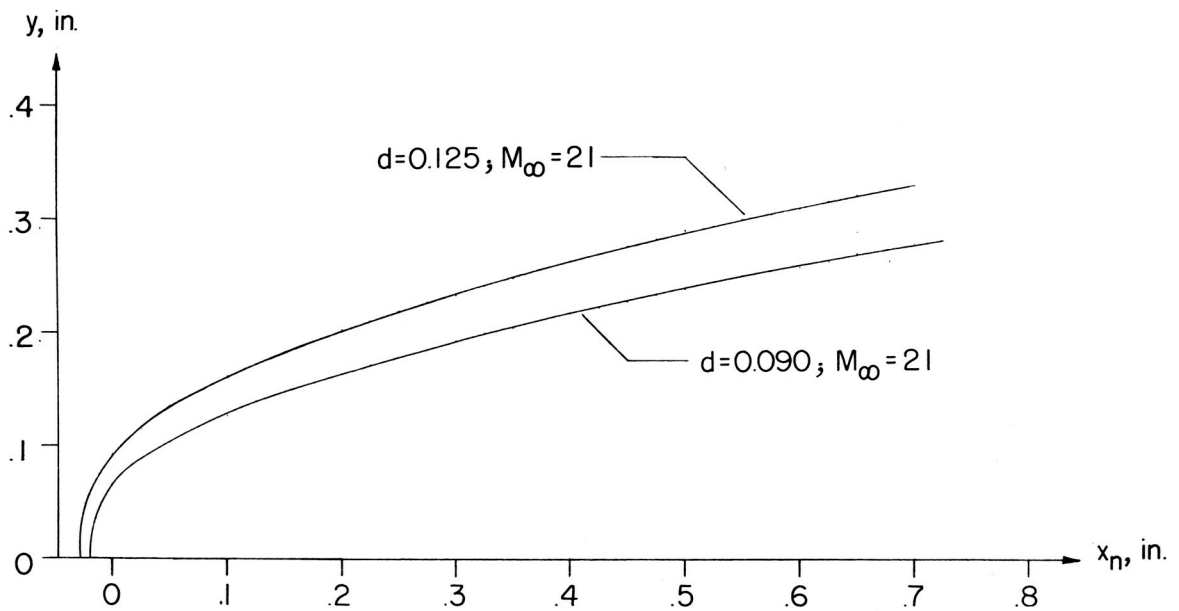


(b) Shock-wave shape.

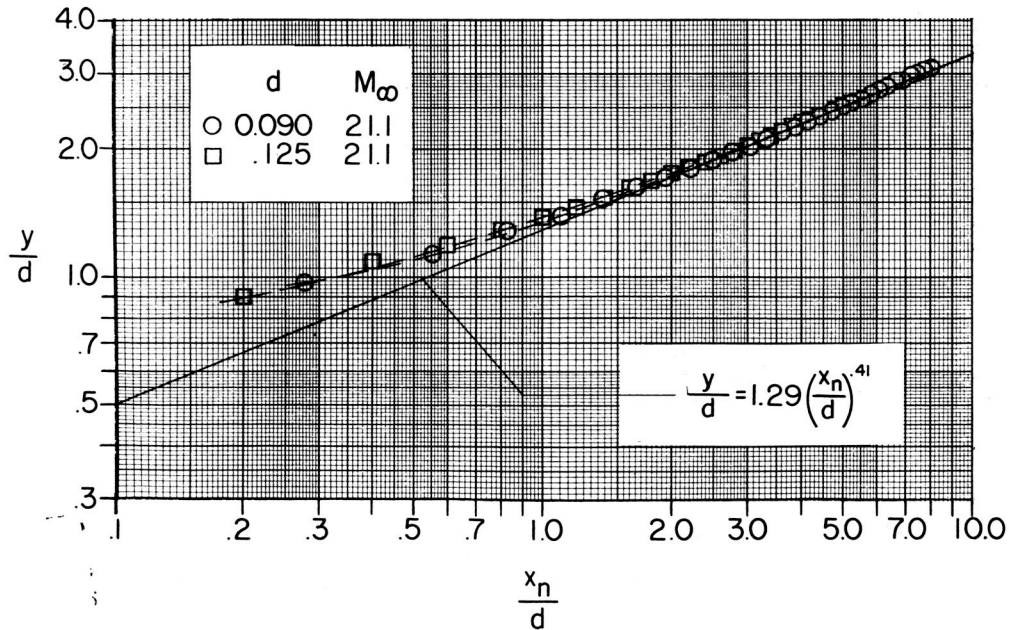


(c) Shock-wave coordinates.

Figure 20.- Shock-shape characteristics on the flat-face model.
 $d = 0.090 \text{ inch}$; $M_\infty = 21$.



(a) Shock-wave shape.



(b) Shock-wave coordinates.

Figure 21.- Comparison of shock-shape characteristics on two flat-nose models.

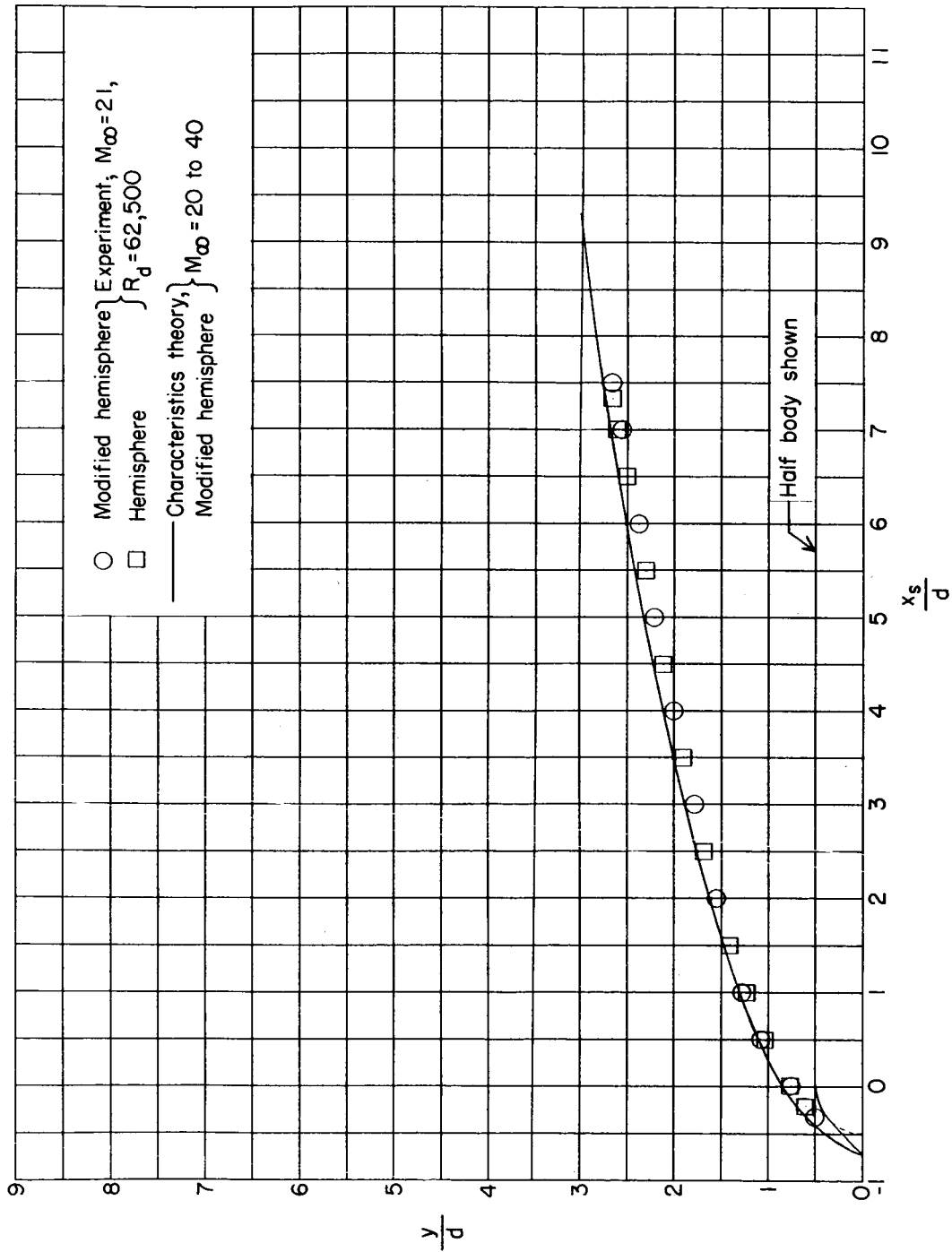


Figure 22.- Comparison of experimental shock shapes with calculated shock shape by the method of characteristics.

